Phil. Trans. R. Soc. Lond. A **323**, 449–469 (1987) [449]
Printed in Great Britain

INTERFACIAL EFFECTS IN THE FLOW OF VISCOUS AND ELASTICOVISCOUS LIQUIDS

BY D. M. BINDING[1], K. WALTERS[1], J. DHEUR[2] AND M. J. CROCHET[2]

[1] *Department of Mathematics, University College of Wales, Aberystwyth, SY23 3BZ U.K.*
[2] *Unité de Mecanique Appliquée, Université Catholique de Louvain, Louvain-la-Neuve, Belgium*

(*Communicated by Sir Granville Beynon, F.R.S. – Received* 6 *May* 1986)

[Plates 1–11]

CONTENTS

A technique of flow visualization by means of an expanded laser beam and trace amounts of particulate additives is used to study the behaviour of newtonian and non-newtonian elastic liquids in complex geometries. Differences in response are highlighted between the newtonian and non-newtonian fluids when these flow separately in certain contraction flows and also in a two-dimensional T geometry. This information is then used to interpret the behaviour when both types of fluid flow together in the same geometry with a well-defined interface between them. Of major interest is the observation that a newtonian liquid in the two-liquid situation (the other liquid being non-newtonian) can behave as if it were highly elastic. We are led to associate this behaviour with the boundary conditions existing at the interface between the newtonian and the non-newtonian liquids.

Powerful finite-element numerical techniques are used in an attempt to simulate the observed flow characteristics. The techniques are able to meet the challenges posed by the two-liquid situation when *both* liquids are newtonian. They are also

able to simulate the distinctive vortex structure observed when only one highly elastic liquid is used in the experiments. They are, as yet, unable to meet the difficult challenge where one of the two liquids is highly elastic.

The experimental and theoretical work has an obvious potential application to the important practical problem of 'coextrusion'.

1. Introduction

This is essentially the third paper in a series which is attempting to understand the way newtonian and non-newtonian elastic liquids behave in complex geometries. For convenience, the previous papers by Cochrane *et al.* (1981) and Walters & Webster (1982) will be referred to as parts 1 and 2, respectively. These papers contained many examples of how elastic liquids can behave in a dramatically different fashion to newtonian liquids. Some of the major conclusions reached were the following.

(i) Fluid inertia and fluid elasticity can often be opposing influences in the sense that increasing the Reynolds number R is equivalent in qualitative terms to decreasing the relevant elasticity number W.

(ii) Small asymmetries in the flow geometry can often have more than a proportionate influence on flow characteristics in the case of highly elastic liquids.

(iii) The precise shape of re-entrant corners (i.e. whether they are sharp or in some sense 'rounded') can have a significant influence on flow characteristics in the case of highly elastic liquids.

(iv) Finite-difference techniques can often be used to advantage to predict the observed flow characteristics, although these techniques are limited by the well known 'high Weissenberg number problem' (see, for example, Crochet & Walters 1983; Crochet *et al.* 1984). The numerical algorithms invariably become unstable and break down at some relatively small value of the elasticity number. This limitation is not confined to our particular numerical techniques but is common to all numerical simulation studies in what is a rapidly expanding research field.

The present paper seeks to add yet more experimental results to supplement those given in parts 1 and 2, but, unlike the earlier work, a major emphasis of the present study concerns the way *two* fluids, with different material properties, interact when they are made to flow in a complex geometry with a well defined interface between them. Some experimental results are provided for the case when two *newtonian* liquids are used, but the most provocative situation is when one newtonian and one highly elastic non-newtonian liquid are used in the experiments.

Simulating the observed flow characteristics in the two-fluid situation involves, among other things, the important task of determining the location of the interface between the fluids, which is certainly not known *a priori*. Although finite-difference techniques based on body fitted coordinates would be appropriate for solving the present problems, we have resorted instead to finite-element techniques (see §5).

2. Test fluids

Experiments have been carried out on fluids with three distinct types of behaviour. First, newtonian fluids, which in our case were mixtures of water and maltose syrup (C.P.C., U.K.). For convenience, we associate the letter N with the newtonian liquids and give the relevant densities and viscosities in table 1.

Secondly, we used so-called Boger fluids (see, for example, Boger 1977/78; Jackson *et al.* 1984), these being fairly dilute (~ 0.1 vol. %) solutions of polyacrylamide (Magnafloc E10 supplied by Allied Colloids (U.K.) Ltd.) in a maltose syrup–water solvent.

Thirdly, an *aqueous* solution of polyacrylamide was used in some of the experiments, having a higher concentration (1 vol. %) than that used in making up the Boger fluids. For convenience, we refer to the Boger fluids as the B series and assign the letter P to the aqueous polyacrylamide solution.

The B and P series are both examples of non-newtonian elastic liquids, but there are important differences between the two. To explain the most obvious differences, we refer to a steady simple shear flow with velocity components referred to a cartesian reference frame given by

$$v_1 = qx_2, \quad v_2 = v_3 = 0, \tag{1}$$

where q is a constant velocity gradient or shear rate. The corresponding stress distribution is given by

$$\left.\begin{aligned} p_{12} &= \tau = q\eta(q), \\ p_{11}-p_{22} &= \nu_1(q), \quad p_{22}-p_{33} = \nu_2(q), \end{aligned}\right\} \tag{2}$$

where the p_{ik} are the components of the stress tensor, τ is the shear stress, η the apparent viscosity, and ν_1 and ν_2 are the first and second normal stress differences, respectively. For the newtonian fluids, it is well known that η is a constant and ν_1 and ν_2 are both zero. For the Boger fluids, the solvent is relatively viscous and the polymer concentration low, so that it is again found that η is (approximately) constant, although, now, the normal stress differences ν_1 and ν_2 are not necessarily zero. Available experimental evidence would suggest that ν_2 is very small and can be taken to be zero within experimental error (cf. Keentok *et al.* 1980), but ν_1 can be very high indeed (Boger 1977, 1978; Jackson *et al.* 1984). In fact ν_1 can be higher than the shear stress τ indicating substantial viscoelastic behaviour. ν_1 is often found to be (approximately) a quadratic function of the shear rate representing so-called second-order behaviour and it is possible to define two material parameters for the Boger fluids, namely the viscosity η and characteristic relaxation time λ through the equations

$$\tau = \eta q, \quad \nu_1 = 2\eta\lambda q^2. \tag{3}$$

Values of the density ρ, η and λ for the Boger fluids used in this study are given in table 2.

Boger fluids are noted for high stresses in stretching flows and also for some anomalous time-dependent antithixotropic behaviour at relatively high shear rates in steady shear flow. Details of these and other non-newtonian effects may be found in Jackson *et al.* (1984) (see also Choplin *et al.* 1983).

For the newtonian and Boger fluids, it is possible to define two non-dimensional numbers R and W, given by

$$R = \rho UL/\eta, \tag{4}$$

$$W = \lambda U/L, \tag{5}$$

where U is a characteristic velocity and L is a characteristic length. R is the usual Reynolds number and W is an elasticity number, sometimes called the Weissenberg number. Clearly, for newtonian liquids $W = 0$. In some of the two-liquid situations, we find it more convenient to simply quote the mean flow rate in each liquid.

The Boger fluids have proved to be popular test fluids in non-newtonian fluid mechanics

TABLE 1. DENSITY AND VISCOSITY FOR NEWTONIAN LIQUIDS

fluid	density, P / g cm^{-3}	viscosity / Pa s
N4	1.35	3.53
N5	1.35	2.63
N6	1.35	2.96
N8	1.36	9.73
N9	1.36	4.43
N10	1.33	3.5
N11	1.32	2.0

TABLE 2. ESTIMATED DENSITY, VISCOSITY AND RELAXATION TIME FOR BOGER FLUIDS

fluid	density, ρ / g cm^{-3}	viscosity, η / Pa s	λ/s
B44	1.36	6.6	0.29
B45	1.32	0.67	0.08
B46	1.35	2.07	0.16
B47	1.35	2.66	0.07
B49	1.35	2.32	0.24

on account of their constant viscosity, which makes it possible to define an unambiguous Reynolds number. Changes in flow characteristics between newtonian and Boger fluids at the same Reynolds number can then be associated with viscoelastic effects.

It is difficult to define a convenient Reynolds number for the more conventional polymer solution P, which at the concentration level used shows marked viscosity variation with shear rate. In fact, the viscosity can fall dramatically with shear rate, giving rise to so called 'shear-thinning' behaviour. For the P solution, we choose to simply quote the relevant mean flow rates in the present study.

Viscometric functions obtained from a Weissenberg Rheogoniometer (R16 model) for the 1% aqueous solution of polyacrylamide are displayed in figure 1. The relevant temperature (20 °C) is that used in all the experiments of the present study.

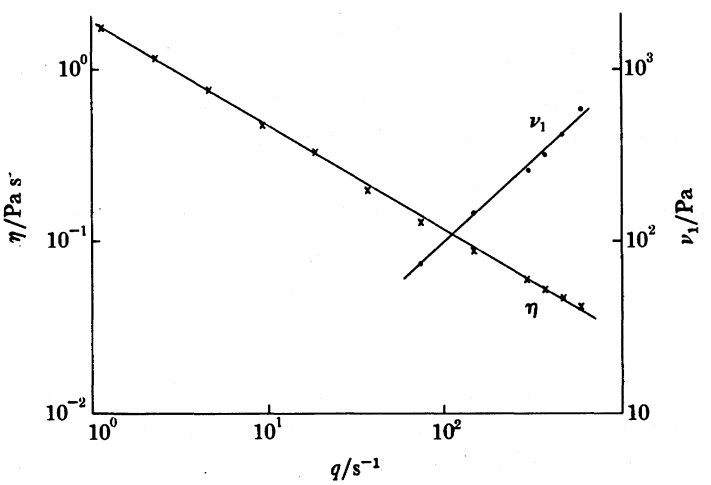

FIGURE 1. Viscometric data for the 1% aqueous solution of polyacrylamide, P. Temperature is 20 °C.

3. Experimental technique

A schematic diagram of the basic apparatus is given in figure 2. The fluids from reservoirs A_1 and A_2 are circulated by means of Watson–Marlow type HRSV variable flow rate peristaltic pumps B_1 and B_2. Two damping bottles C_1 and C_2 act as buffers and smooth out the two flows. The flows interact in the test section D and the mixture finds its way into the disposal container E. When the liquids in reservoirs A_1 and A_2 are the same, it is of course possible to recycle the fluid.

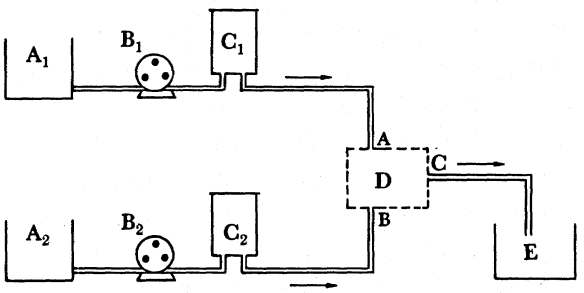

Figure 2. Schematic diagram of the basic experimental apparatus.

Flow rates are measured by a conventional catch and weigh technique. The geometries used in the test section are shown schematically in figure 3. The original T geometry, (figure 3*a*), had a depth of 20 mm, but in later experiments one with a depth of 60 mm was available (figure 3*b*). This was constructed to ensure that the substantial changes in flow characteristics due to viscoelasticity observed in the original T geometry were not due to any three-dimensional effect brought about by the short depth of the apparatus. That three-dimensional effects were absent in the original geometry was also investigated by varying the plane of flow observation (see figure 11).

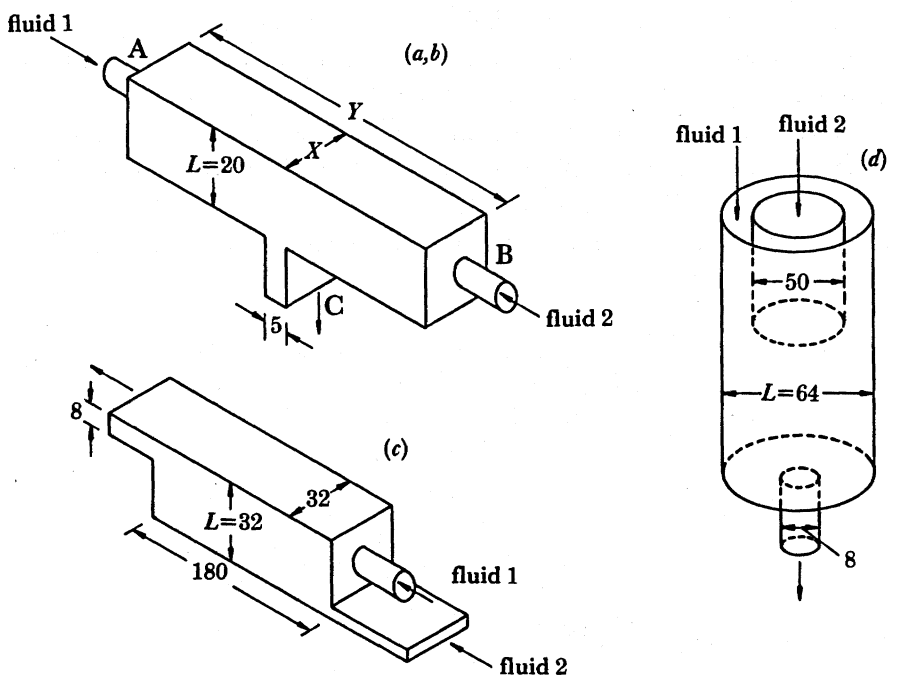

Figure 3. Schematic diagrams of the geometries. (*a*) T geometry, $X = 20$, $Y = 750$; (*b*) T geometry, $X = 60$, $Y = 510$; (*c*) planar-step geometry; (*d*) axisymmetric geometry. All dimensions are in millimetres.

We estimate that all the arms to the T geometries were of sufficient length to ensure that 'fully developed' conditions existed at both entrance and exit. Whereas the T geometry keeps the two fluids separated until immediately before the contraction that is at 90° to the initial flow, the planar step geometry (figure 3*c*) allows the fluids to flow as two adjacent layers before passing through the contraction.

The axisymmetric geometry (figure 3*d*) consists of two concentric cylinders and was constructed in such a way as to allow the inner cylinder to be placed at any distance from the contraction. The final placement in the present experiments was chosen to allow the flow to become 'fully developed' in the region above the contraction.

In figure 3 the characteristic length L used in the calculation of the Reynolds and Weissenberg numbers is indicated for each of the geometries used. Notice that L relates to an 'upstream' position, i.e. a position reached by the fluid *before* it passes through the contraction. Characteristic velocities were estimated by the following procedure for the constant viscosity fluids. First the total volumetric flow rate was measured at the outlet of the geometry. Then, from the photograph of the flow field, a region of fully developed flow was isolated and the position of the interface between the two fluids determined. Standard formulae for Poiseuille flow and Couette flow were then used to determine the flow rates of the individual fluids.

As in previous papers, we have resorted to a simple visualization technique, which requires only trace amounts of particulate additives and which uses an expanded laser beam as illuminating source (figure 4). A 5 mW helium–neon laser was spread into a narrow sheet of light by means of a cylindrical lens and the flow captured by taking photographs with suitable time exposures. The principle of the method is simple. Small particles, contained in and moving affinely with the flow, give a visual representation of the flow as they are illuminated by the laser light and photographed. In the present study, we used polyvinyl chloride particles with a density of 1.4 g cm^{-3} in connection with the newtonian and Boger fluids and a high-density polyethelyne powder (Hoechst, U.K.) with a density of 0.94 g cm^{-3} for the aqueous polyacrylamide solutions. We found it convenient to use 2 g of powder in every 10 l of test fluid.

Because the grain size of the powders, when in suspension, was of the order of 0.1 mm in diameter, it was our reasonable expectation that the particles faithfully followed the streamlines. In the vast majority of the present experiments, we believe that this was indeed so. However, there is evidence that in some parts of the flow field, where the flow is very strong, the particles could not follow the streamlines (cf. figure 9).

For completeness we note that in the present study no *interfacial* instabilities were discernible.

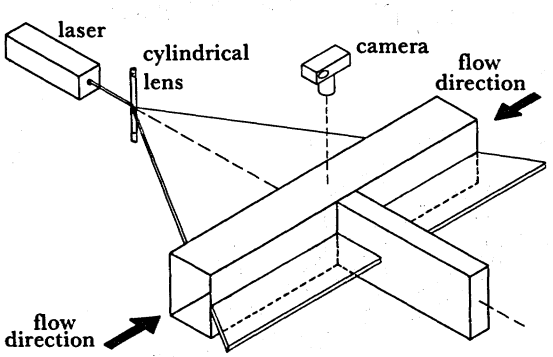

FIGURE 4. Schematic diagram of the laser-based visualization system.

4. Experimental results

(i) *The* T *geometry (one liquid)*

We consider first the T geometry (figure 3*a*). Confirmation that the flow characteristics observed were two-dimensional effects was provided by an occasional movement of the laser beam from its central position to positions nearer one of the bounding walls. Further confirmation was provided by complementary experiments in the wider geometry (figure 3*b*).

In figures 5–9, plates 1–5, only one liquid is used in each experiment and the way viscous and elasticoviscous liquids behave when the T geometry is used as a main channel with a right-angle bypass connection is shown in figure 5. Here, there is only one feeder arm (A) with two exit arms (B and C). The newtonian liquids found no difficulty negotiating the abrupt change in direction near the bypass. In contrast the elastic liquids exhibited a characteristic overshoot. Such an overshoot is a common feature of the behaviour of elastic liquids in many flows (see, for example, Walters 1975) but the overshoot shown in figure 5*b* is certainly a severe example of the phenomenon.

For the majority of the experiments in the T geometry, the fluids were supplied through *two* of the arms (A and B) and the impinging streams then flowed through the remaining arm (C). Figure 6 contains representative data for newtonian fluids. Over the available range of flow conditions, no distinctive features were observed except when flow in one of the entry arms was stopped (or was extremely slow). The usual exposure time of 8 s was insufficient to capture any vortex behaviour in figure 6*a*, but when this exposure time was increased to 8 min 32 s, the structure of the very weak recirculating vortex became evident (figure 6*b*).

In figure 6*c*, *d* the main interest lies in the position of the dividing streamline between the two liquid streams.

The relatively uninteresting newtonian experiments are in marked contrast to those for the Boger fluids, which are summarized in figure 7. Here, there are strong vortices present in all but the symmetrical case. The vortices occur near the lip in the arms containing the slower moving fluid. Interestingly, the vortices essentially disappear when the flow rates in the entry arms are balanced, although, even in this case, the streamlines have a different shape to those found in the corresponding newtonian experiments.

The shear thinning P liquids also exhibit vortices in the T geometry (figures 8 and 9). The streamlines in the wider T geometry given in figure 8 show clearly the presence of *two* recirculating vortices *even when the flow rates in the two entry arms are the same.* This is in marked contrast to the experiments for the B series elastic liquids.

In the experiments shown in figure 9 there is a marked flow instability, which is especially evident within the vortex region. Also noteworthy in figure 9 is the obvious conglomeration of trace particles with a consequential particle-free region. The flow is apparently so strong in this region as to prevent the tracer particles being transported with the fluid, an example of the so-called Uebler effect (cf. Metzner *et al.* 1969).

(ii) *The* T *geometry (two liquids)*

In all the experiments reported here, we are confident that over the timescale of the experiments, the fluids could be considered to be immiscible.

Figure 10, plate 6, contains photographs of the streamlines when two different newtonian liquids flow in the entry arms. The flow is very similar to that found in the one-newtonian-liquid

situation with no added flow characteristics worthy of mention, except that there is enough evidence in the figure to indicate that a knowledge of the Reynolds numbers alone in the respective arms is not sufficient to define the flow. It is certainly necessary to know the individual viscosities.

We note that the recirculating vortex in figure 10*c* is not generated by the viscoelastic lip vortex mechanism, which is so prevalent in the flow of elastic liquids (see, for example, Evans & Walters 1986; Boger *et al.* 1986) and is responsible for the vortices in figures 7–9. Rather, the vortex in figure 10*c* is a residual of the large weak vortex which is present when flow in one arm is stopped.

Of significant interest is the behaviour in the T geometry when one of the liquids is newtonian and the other is from the B series. Figure 11, plate 7 contains representative photographs for this situation. Here, strong recirculating vortices are found in the *newtonian* liquid, which is behaving as if it were a highly elastic liquid (figure 11*a*, *c*). We must associate this unusual behaviour with the (obviously severe) conditions at the interface between the two fluids.

Figure 11*c*, which was taken near the base of the geometry for the same conditions as those in figure 11*b* is included to confirm that the effect in the latter is two dimensional.

Figure 11*d* shows that if the flow in the newtonian liquid is strong enough, a vortex can be generated in the slower moving Boger fluid.

The photographs in figure 11*a*, *d* have the same general shape as those found when the same Boger fluid flows through each entry arm (figure 7) and the newtonian liquid in figure 11 is certainly behaving as if it were an elastic liquid.

(iii) *The planar step geometry* (figure 3*c*)

Figure 12*a*, plate 8, is a photograph of streamlines for a newtonian fluid flowing over a step and figure 12*b*, plate 8, for a Boger fluid, shows that conditions can be obtained for which the flow is similar to the newtonian situation (cf. part 2). However, in contrast to newtonian fluids, the Boger fluids may also exhibit a recirculating vortex near the lip of the contraction (figure 12*c*, plate 8) or, at slightly higher flow rates, a vortex occupying a large region in the salient corner. (The camera position used in this geometry means that there is a small three-dimensional photographic effect that is evident near the step.) The vortex in figure 12*c* is a further example of the lip vortex mechanism which has been studied in detail by Evans & Walters (1986) and Boger *et al.* (1986).

When a Boger fluid and a newtonian fluid are used in the step geometry, we can again obtain a vortex in the newtonian fluid (figure 13, plate 9), which is certainly not obtainable without the influence of the Boger fluid and which is of a shape that is unattainable for any other liquids or for any other conditions that we have been able to study in the one-liquid case. Figure 13*a*, *b* are in fact further examples of the phenomenon that was emphasized in connection with figure 11.

When the roles of the newtonian and Boger fluids are reversed, the newtonian fluid may force the Boger fluid into the salient corner as is seen in figure 13*c* or it may generate a vortex in the Boger fluid in the salient corner (figure 13*d*). There is now, however, an interesting secondary vortex in the newtonian liquid. Indications are that the flow in this vortex is unstable. Figures 14*a*, *b* and *c*, plate 10, are typical of the flow fields generated when shear thinning fluids flow alongside Boger fluids in the planar step geometry. A vortex is generated in the salient corner in the Boger fluid. In all three cases shown, the flow rate in the Boger fluid is fixed and that of the shear thinning fluid is varied, with little effect on the size of the vortex.

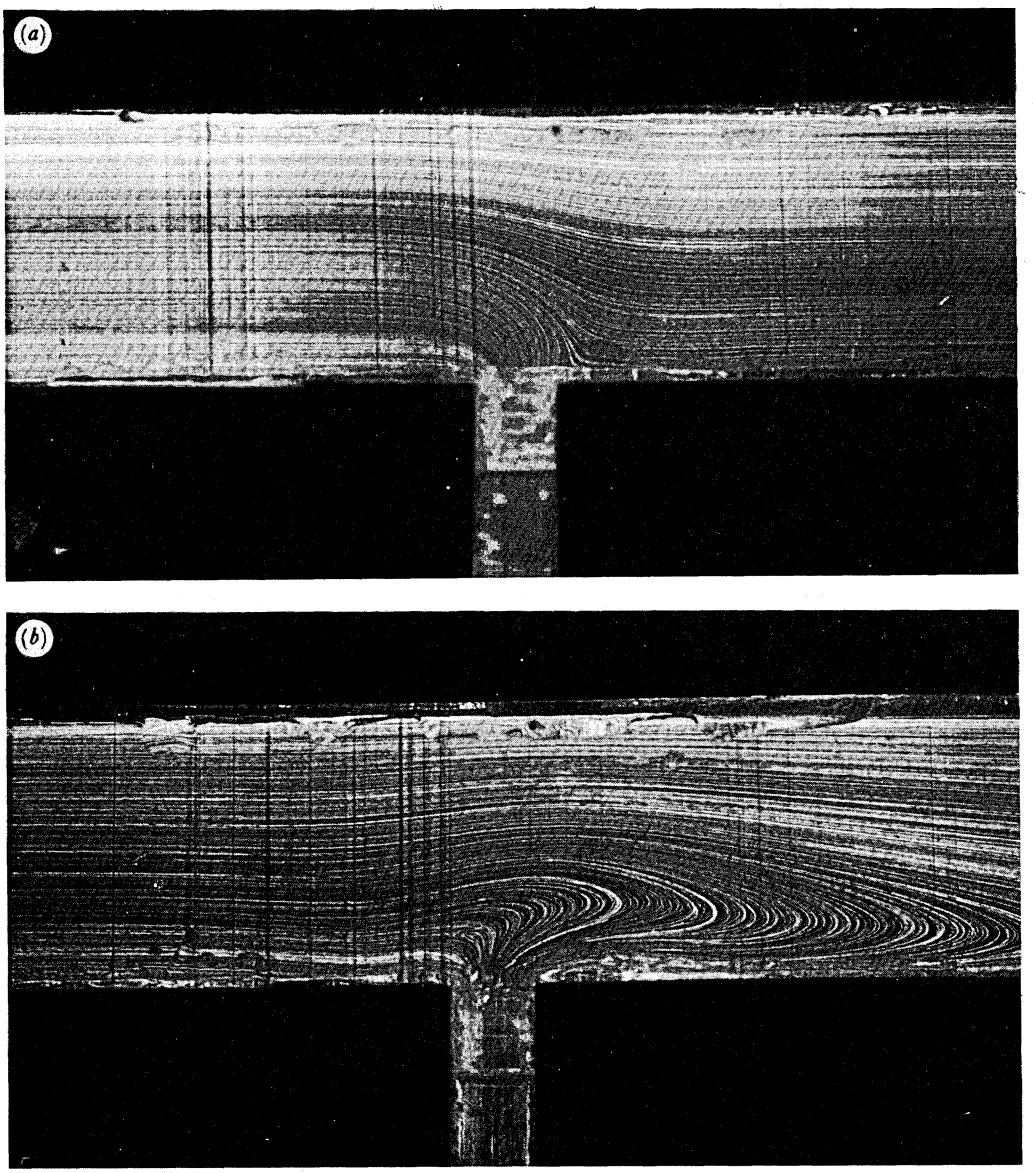

FIGURE 5. T geometry (3*a*) with one fluid. Fluid enters at A and exits at B and C. The R and W numbers are based on inlet conditions. (*a*) Fluid N9, $R = 0.054$, $W = 0.0$; (*b*) fluid B49: $R = 0.071$, $W = 0.29$.

(*Facing p.* 456)

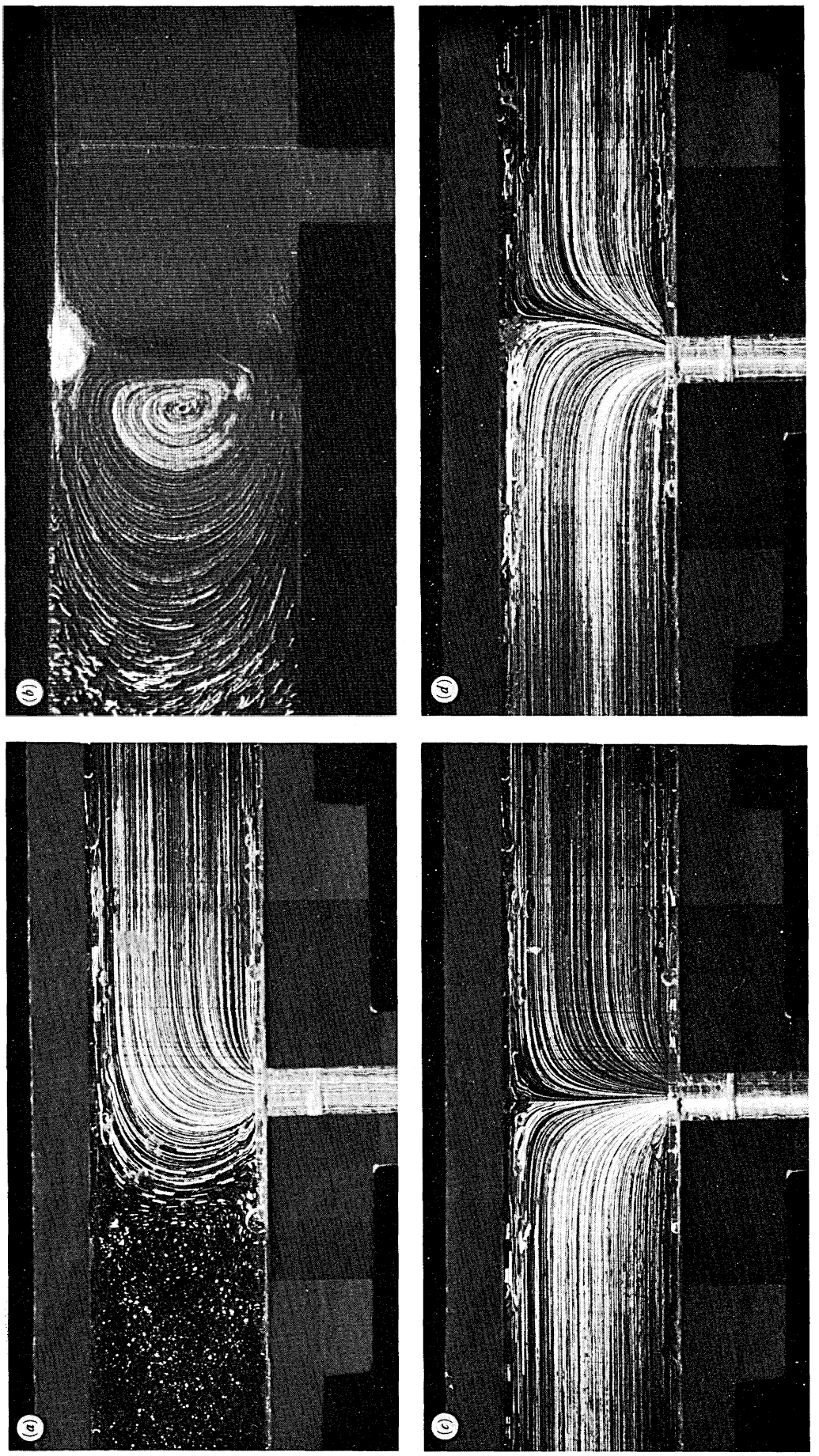

FIGURE 6. T geometry (3*a*) with newtonian fluid N4 entering through arms A and B. (*a*) $R_A = 0$, $R_B = 0.058$, total flow rate is 3.0 ml s^{-1}; (*b*) $R_A = 0$, $R_B = 0.058$, total flow rate is 3.0 ml s^{-1}; (*c*) $R_A = 0.058$, $R_B = 0.058$, total flow rate is 6.0 ml s^{-1}; (*d*) $R_A = 0.065$, $R_B = 0.028$, total flow rate is 4.8 ml s^{-1}.

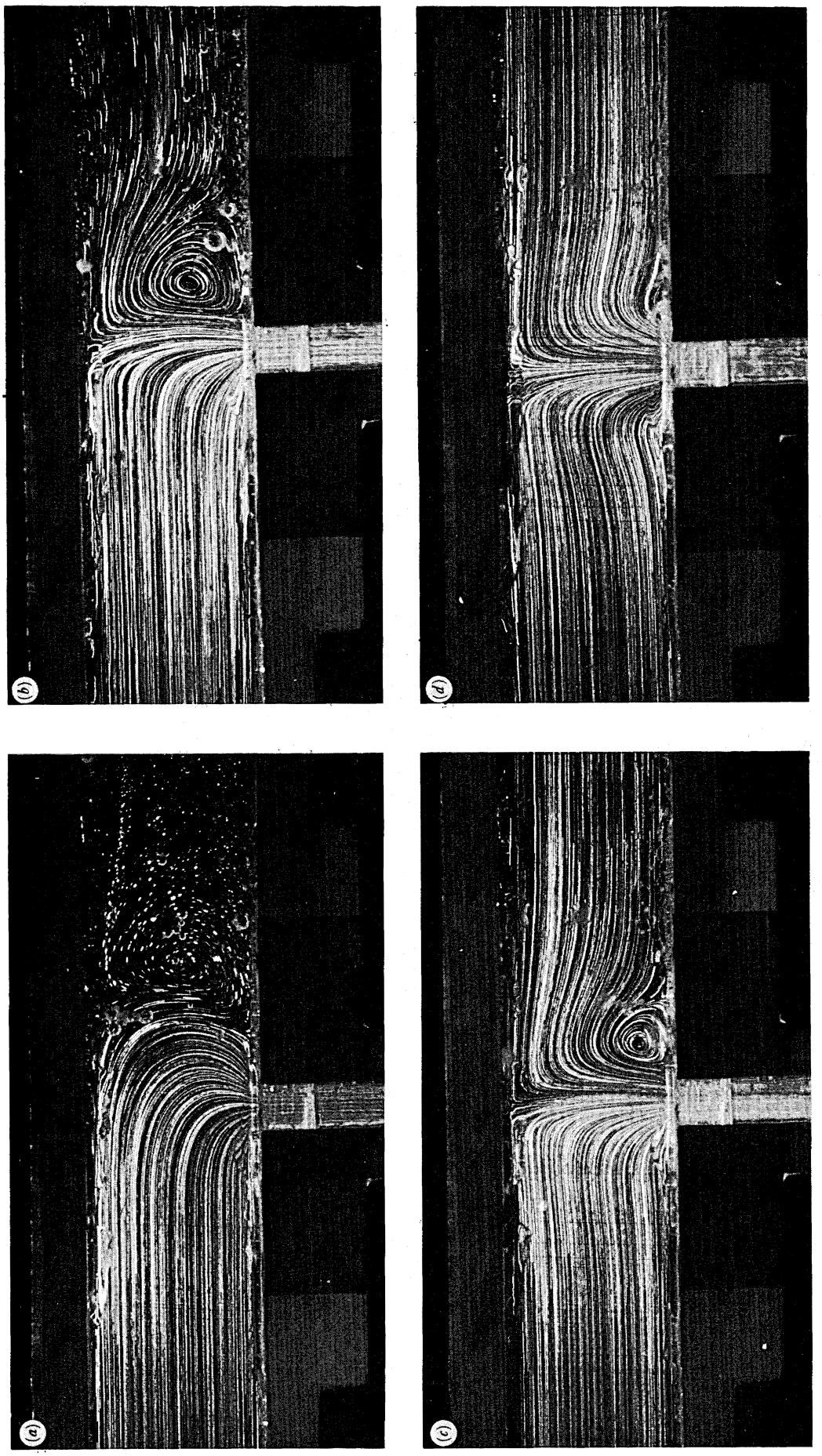

FIGURE 7. T geometry (3*a*) with Boger fluid B44 entering through arms A and B. (*a*) $R_A = 0.16$, $R_B = 0$, $W_A = 0.055$, $W_B = 0$, total flow rate is 1.6 ml s^{-1}; (*b*) $R_A = 0.016$, $R_B = 0.004$, $W_A = 0.053$, $W_B = 0.013$, total flow rate is 1.95 ml s^{-1}; (*c*) $R_A = 0.012$, $R_B = 0.008$, $W_A = 0.04$, $W_B = 0.026$, total flow rate is 1.95 ml s^{-1}; (*d*) $R_A = 0.014$, $R_B = 0.014$, $W_A = 0.048$, $W_B = 0.048$, total flow rate is 2.8 ml s^{-1}.

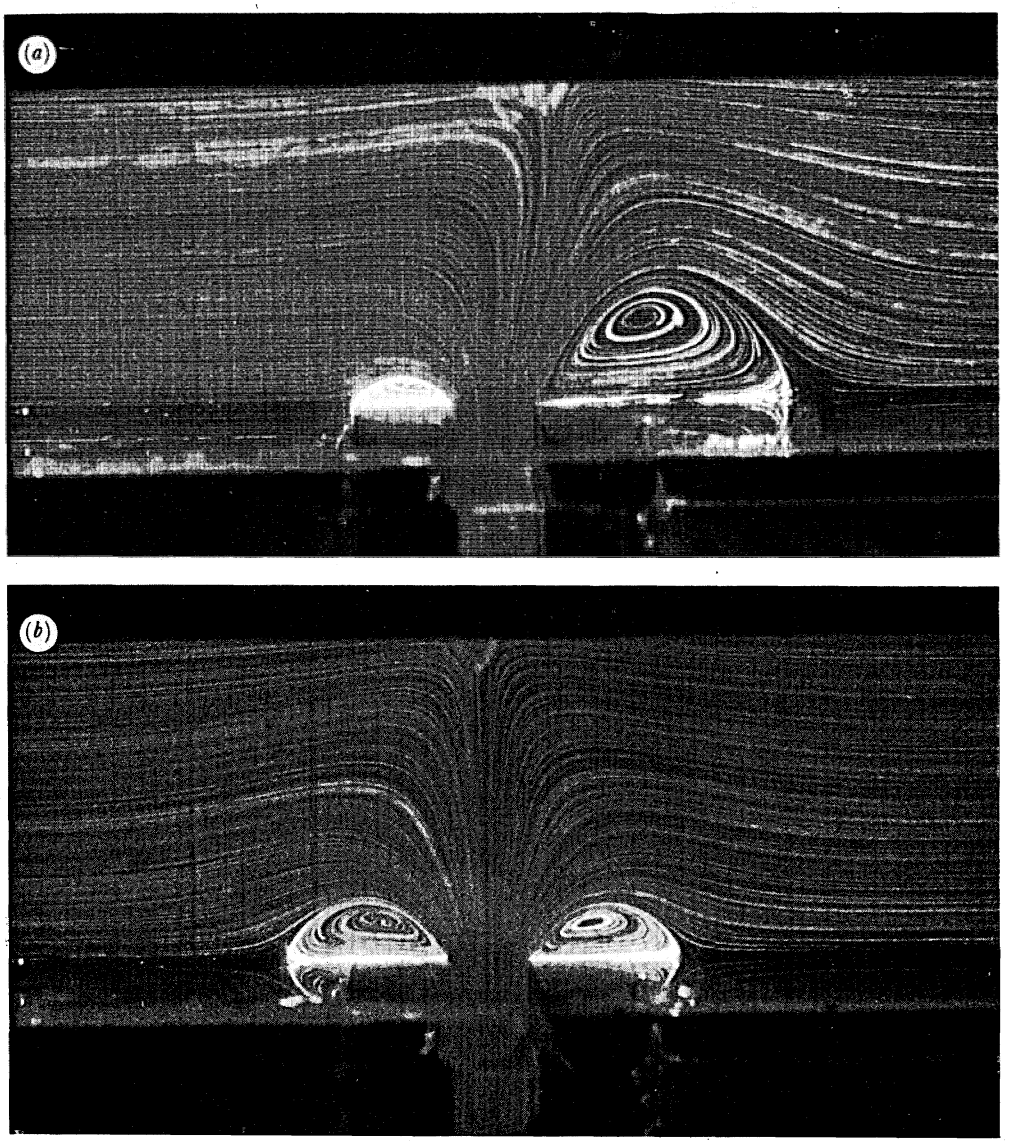

FIGURE 8. T geometry (3*b*) with shear thinning fluid P entering through arms A and B. (*a*) $Q_A = 49.1$ ml s^{-1}, $Q_B = 22.3$ ml s^{-1}; (*b*) $Q_A = Q_B = 35.7$ ml s^{-1}.

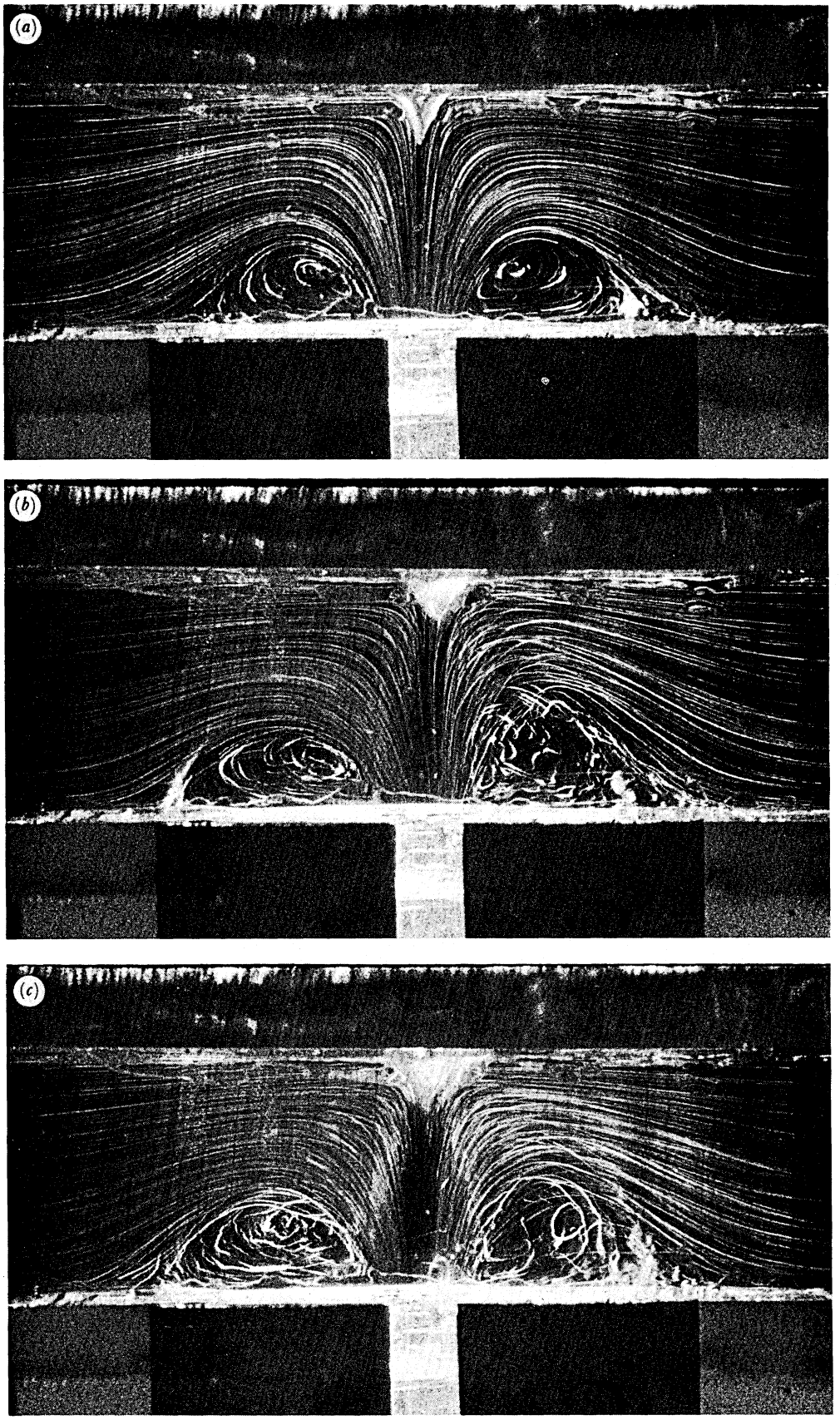

FIGURE 9. T geometry (3*a*) with shear thinning fluid P entering through arms A and B. (*a*) $Q_A = Q_B = 5.2$ ml s^{-1}; (*b*) $Q_A = Q_B = 7.5$ ml s^{-1}; (*c*) $Q_A = Q_B = 10.0$ ml s^{-1}.

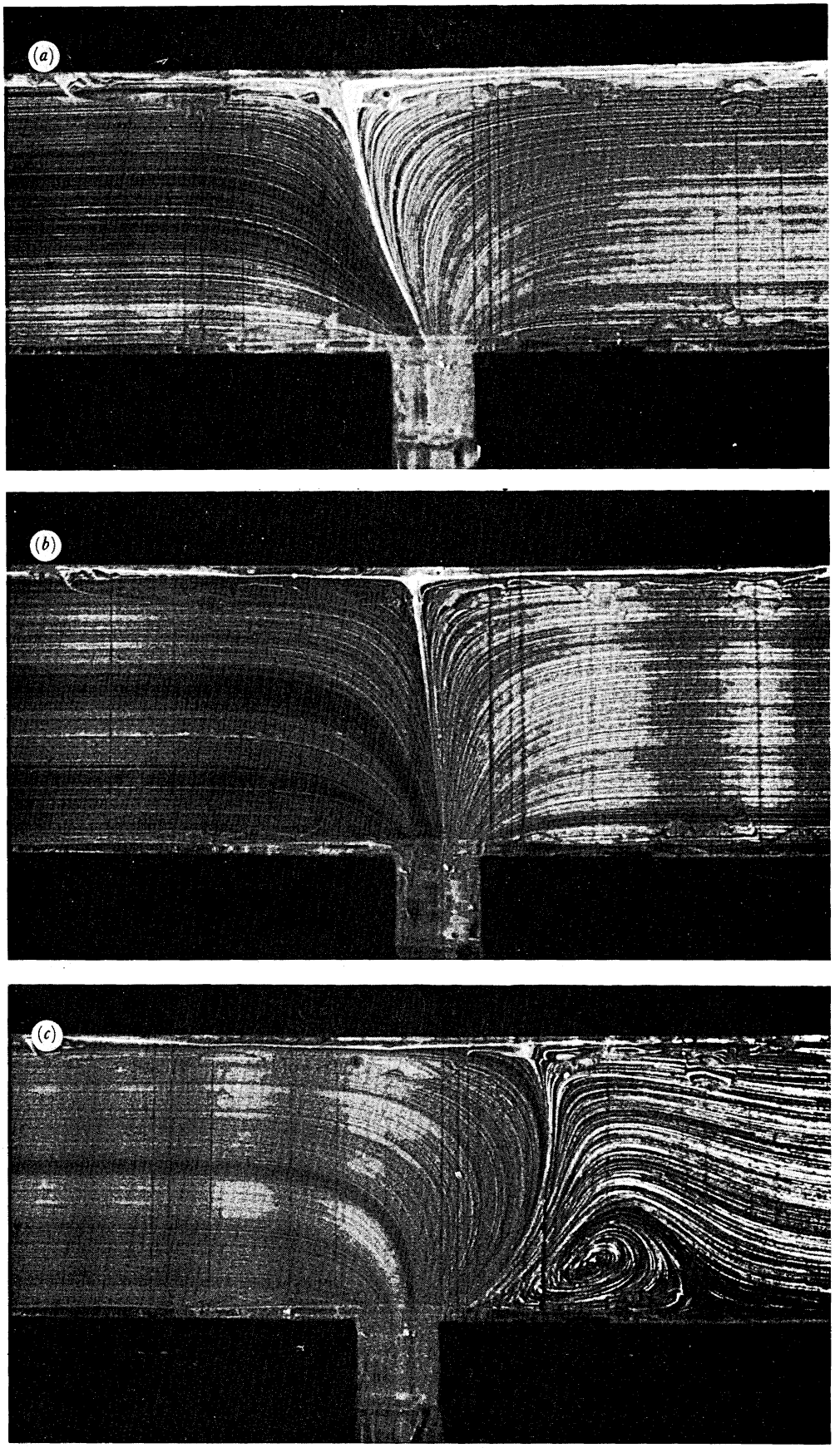

FIGURE 10. T geometry (3*a*) with newtonian fluids N10 and N11 entering through arms A and B, respectively. (*a*) $R_A = 0.09$, $R_B = 0.41$, total flow rate is 18 ml s^{-1}; (*b*) $R_A = 0.14$, $R_B = 0.26$, total flow rate is 15.4 ml s^{-1}; (*c*) $R_A = 0.12$, $R_B = 0.02$, total flow rate is 6.45 ml s^{-1}.

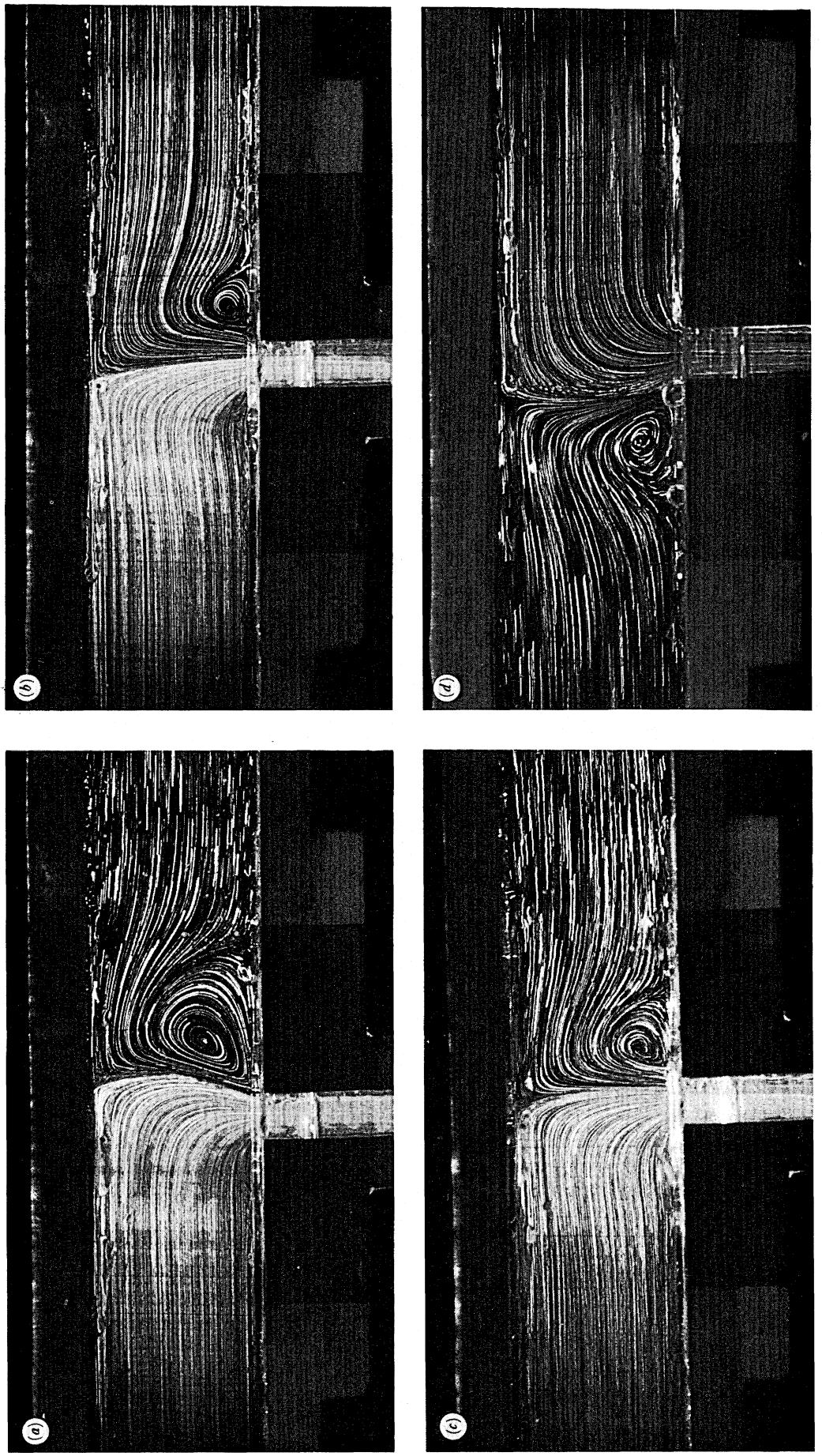

FIGURE 11. T geometry (3*a*) with Boger fluid and newtonian fluid entering through arms A and B respectively. (*a*) Fluid B44, $R_A = 0.018$, $W_A = 0.06$, and fluid N4, $R_B = 0.006$, $W_B \equiv 0$, total flow rate is 2.1 ml s^{-1}; (*b*) fluid B44, $R_A = 0.015$, $W_A = 0.052$, and fluid N4, $R_B = 0.024$, $W_B \equiv 0$, total flow rate is 2.8 ml s^{-1}; (*c*) fluid B44, $R_A = 0.015$, $W_A = 0.052$ and fluid N4, $R_B = 0.024$, $W_B \equiv 0$, total flow rate is 2.8 ml s^{-1}. Plane of laser near rear bounding wall. (*d*) Fluid B45, $R_A = 0.025$, $W_A = 0.002$ and fluid N5, $R_B = 0.037$, $W_B \equiv 0$, total flow rate is 1.0 ml s^{-1}.

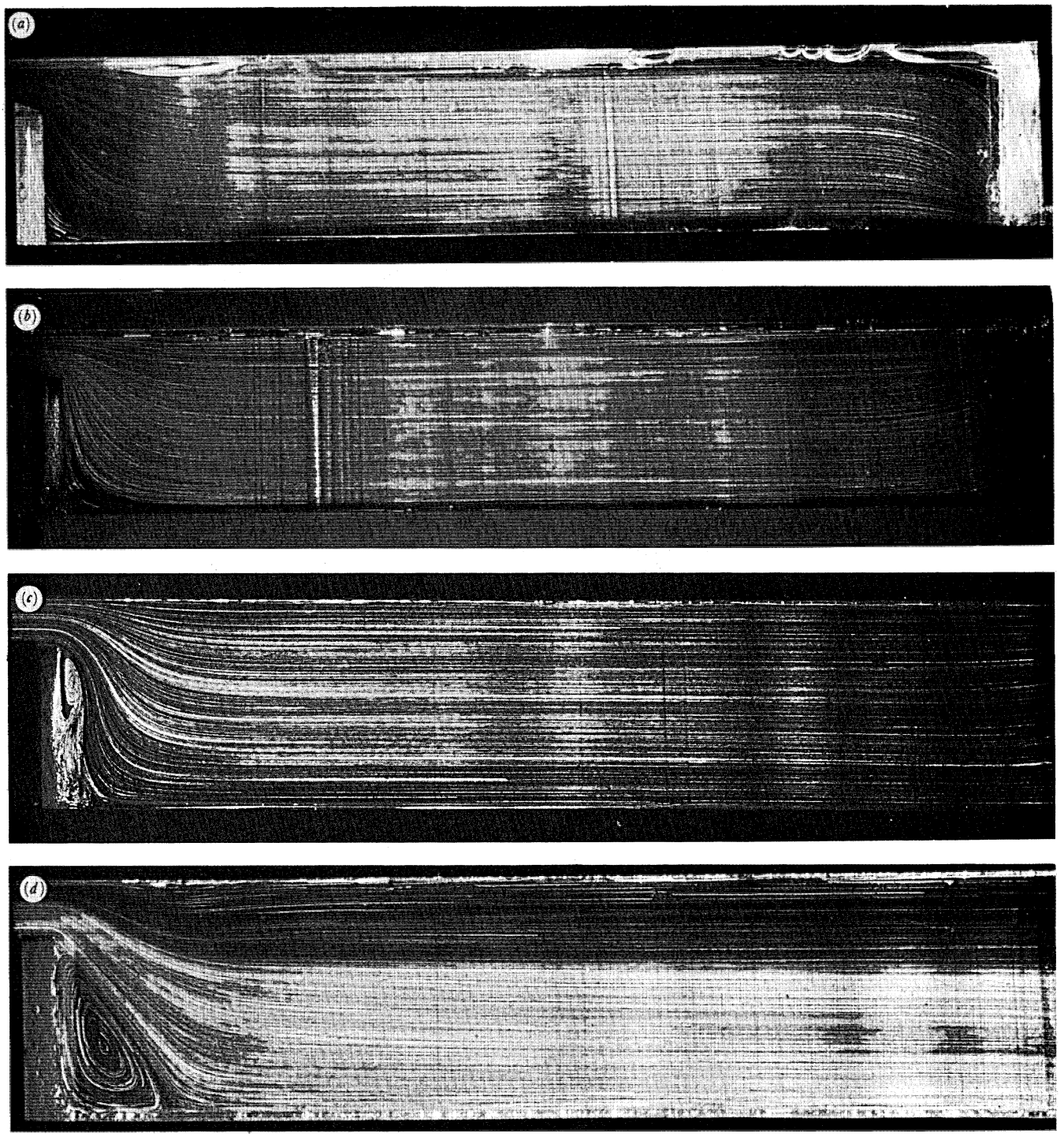

FIGURE 12. Flow patterns for one fluid flowing through the planar step geometry (3*c*). (*a*) newtonian fluid N8, $R = 0.058$, $W \equiv 0$, total flow rate is 13.2 ml s^{-1}; (*b*) Boger fluid B46, $R = 0.11$, $W = 0.027$, total flow rate is 5.5 ml s^{-1}; (*c*) Boger fluid B49, $R = 0.12$, $W = 0.048$, total flow rate is 6.6 ml s^{-1}; (*d*) Boger fluid B49, $R = 0.13$, $W = 0.052$, total flow rate is 7.1 ml s^{-1}.

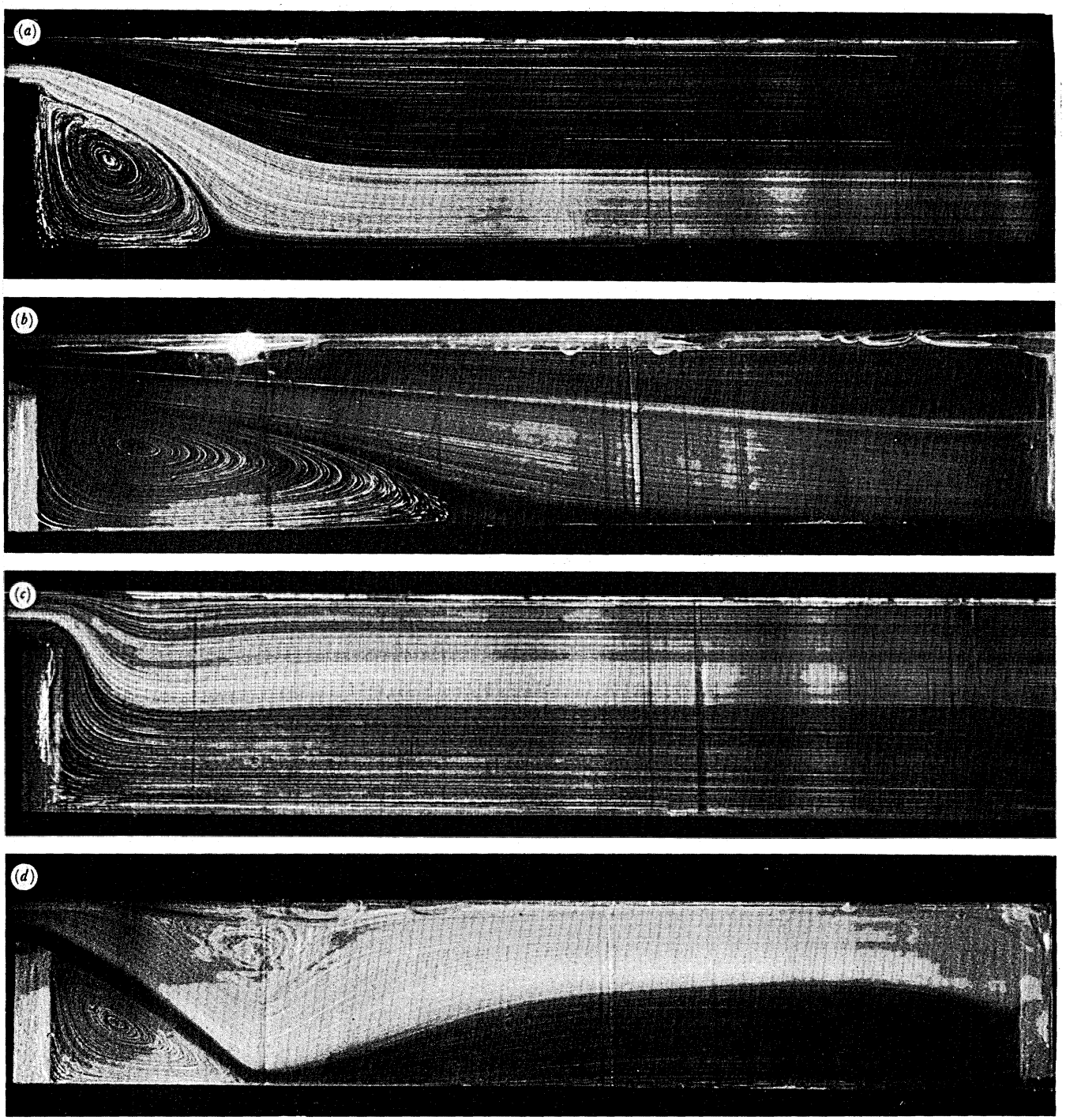

FIGURE 13. Flow patterns for two fluids flowing through the planar step geometry (3*c*). (*a*) Fluid 1 is B49, $Q_1 = 6.2$ ml s^{-1}, fluid 2 is N9, $Q_2 = 5.7$ ml s^{-1}; (*b*) fluid 1 is B47, $Q_1 = 11.8$ ml s^{-1}, fluid 2 is N8, $Q_2 = 13.2$ ml s^{-1}; (*c*) fluid 1 is N9, $Q_1 = 6.3$ ml s^{-1}, fluid 2 is B49, $Q_2 = 6.2$ ml s^{-1}; (*d*) fluid 1 is N8, $Q_1 = 19.7$ ml s^{-1}, fluid 2 is B47, $Q_2 = 11.8$ ml s^{-1}.

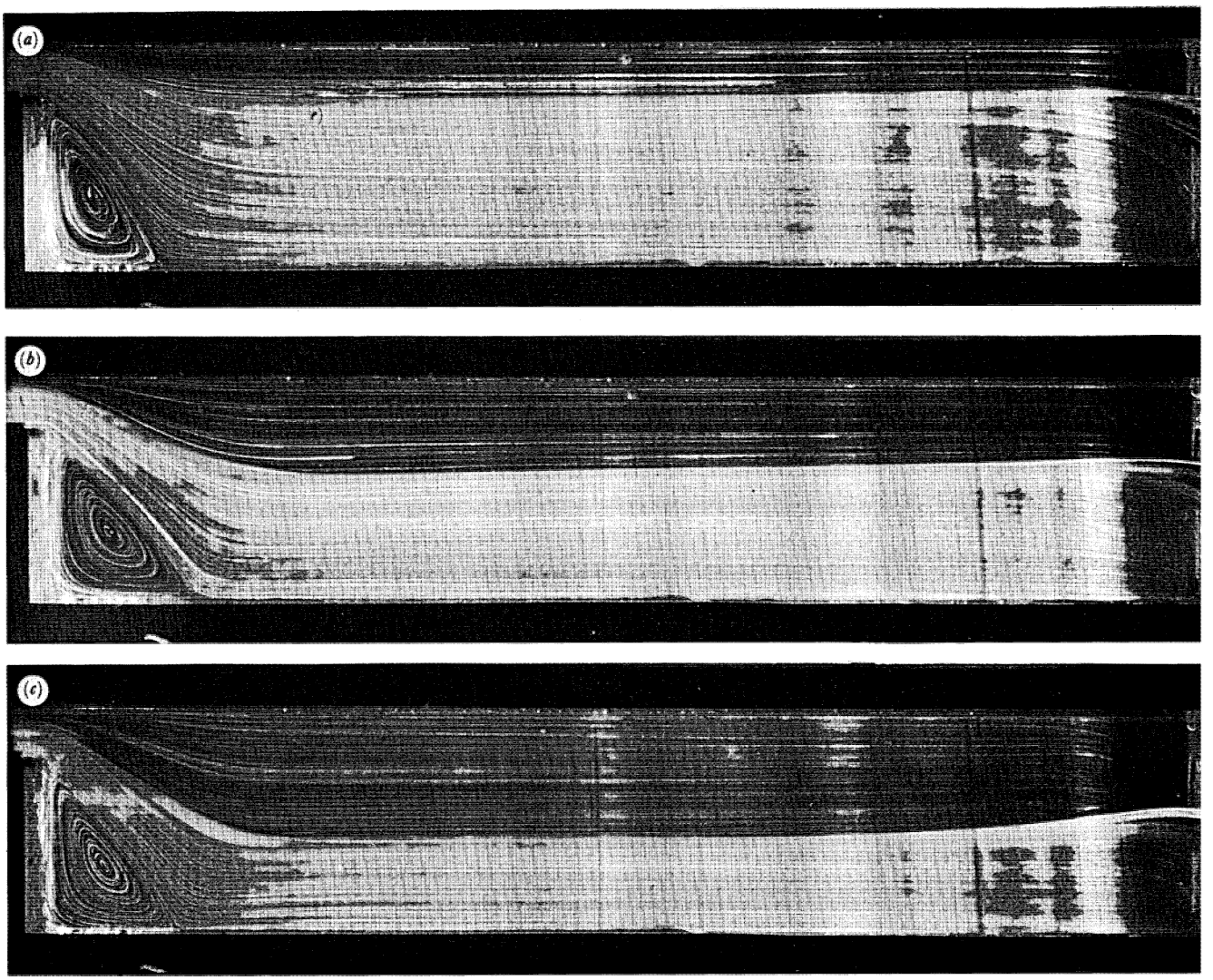

FIGURE 14. Flow patterns for two fluids flowing through the planar step geometry. (*a*) Fluid 1 is P, $Q_1 = 0.3$ ml s^{-1}, fluid 2 is B49, $Q_2 = 6.2$ ml s^{-1}; (*b*) fluid 1 is P, $Q_1 = 5.9$ ml s^{-1}, fluid 2 is B49, $Q_2 = 6.2$ ml s^{-1}; (*c*) fluid 1 is P, $Q_1 = 35.2$ ml s^{-1}, fluid 2 is B49, $Q_2 = 6.2$ ml s^{-1}.

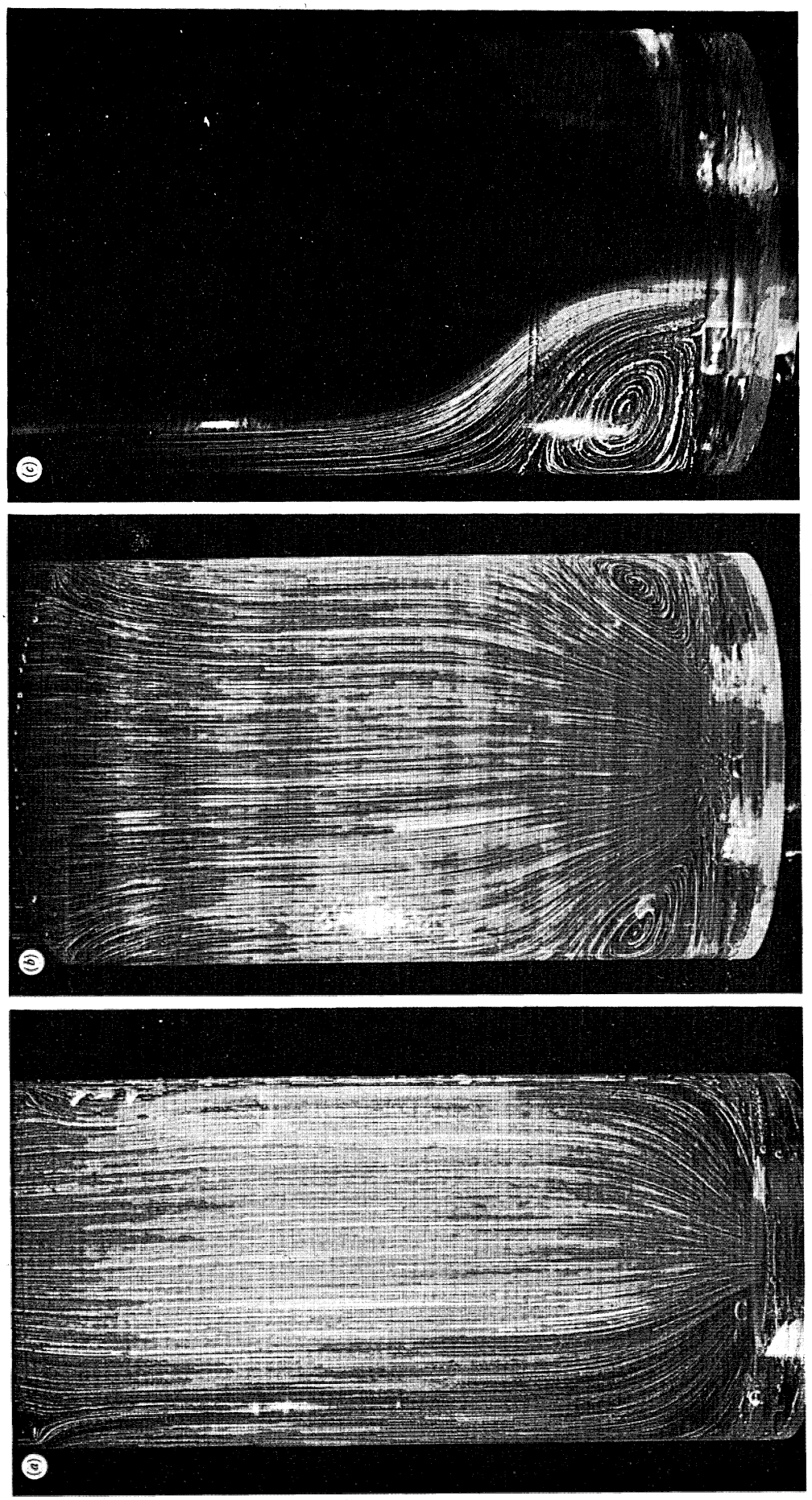

FIGURE 15. Flow patterns for fluids flowing in the axisymmetric geometry (3*d*). (*a*) One fluid, N6, flow rate is 8.1 ml s^{-1}; (*b*) one fluid, B46, flow rate is 18.5 ml s^{-1}; (*c*) fluid 1 is N6, flow rate is 8.0 ml s^{-1}, fluid 2 is B46, flow rate is 8.3 ml s^{-1}.

(iv) *The axisymmetric contraction geometry* (figure 3*d*)

Figure 15 contains photographs for flow in the axisymmetric geometry. Figure 15*a*, plate 11 for the newtonian liquid and figure 15*b*, plate 12 for the Boger fluid are as expected, with characteristic vortex enhancement in the latter. Of more interest in the present context is the case when the Boger fluid is used as liquid (A) and the newtonian fluid as the lubricant (B). We have dyed the Boger fluid to emphasize the flow in the newtonian lubricant. Here again, there is substantial vortex activity in the newtonian liquid, which must be attributable to the strong flow conditions existing at the interface between the two fluids.

5. Numerical methods

(i) *One liquid*

We wish to make use of available numerical methods for simulating the flow of the maltose syrup–water mixtures and the highly elastic Boger fluids. Both types of fluid exhibit an essentially constant viscosity in a steady simple shear flow, but whereas viscoelastic effects cannot be detected in the mixture of water and maltose syrup, they are very strong in the case of the Boger fluids.

The choice of constitutive equation for the maltose syrup–water mixture is straightforward because the fluids are newtonian. We are able to write

$$\mathbf{p} = -p\mathbf{I} + \mathbf{T}, \tag{6}$$

$$\mathbf{T} = 2\eta \mathbf{d}, \tag{7}$$

where $\mathbf{p}$ is the stress tensor, p an arbitrary isotropic pressure, $\mathbf{I}$ the unit tensor, $\mathbf{T}$ is called the 'extra stress tensor', η is the constant viscosity coefficient and $\mathbf{d}$ the rate of deformation tensor defined by

$$\mathbf{d} = \tfrac{1}{2}(\nabla \boldsymbol{v} + (\nabla \boldsymbol{v})^{\mathrm{T}}), \tag{8}$$

where $\boldsymbol{v}$ is the velocity vector and a superscript T denotes the transpose. In (6)–(8), the variables are referred to a fixed rectangular cartesian set of axes.

The choice of constitutive equation for the Boger fluids is less straightforward. It has been customary to employ the so-called Oldroyd B model with equations of state given by

$$\mathbf{T} + \lambda_1 \overset{\nabla}{\mathbf{T}} = 2\eta_0[\mathbf{d} + \lambda_2 \overset{\nabla}{\mathbf{d}}]. \tag{9}$$

η_0 is a constant viscosity coefficient and λ_1 and λ_2 are the relaxation time and retardation time, respectively. The ∇ denotes the upper convected time derivative introduced by Oldroyd (1950). For the steady simple shear flow (1), the stress distribution for the Oldroyd B fluid is

$$\left.\begin{aligned} \tau &= q\eta_0, \quad \nu_1 = 2\eta_0(\lambda_1 - \lambda_2)q^2, \\ \nu_2 &= 0. \end{aligned}\right\} \tag{10}$$

It is clear from the discussion of §2 that the Oldroyd B model is at least adequate to describe the steady simple shear properties of the Boger fluid. However, evidence is now available (see, for example, Jackson *et al.* 1984; Boger *et al.* 1986) that the situation is more complicated than was first imagined. At least two relaxation times are now thought to be preferred (as opposed to the one in the Oldroyd B model) (cf. Boger *et al.* 1986) and there are other complicating

factors such as antithixotropy (cf. Jackson *et al.* 1984). There is clearly a need for a detailed appraisal of the use of relatively simple models to characterize real elastic liquids. This may be a major undertaking with no guarantee of ultimate success. Accordingly, we continue to use the Oldroyd B fluid in the present paper as a reasonably acceptable model for the Boger fluids.

The flow of *one* fluid in the geometries of interest in the present paper can be simulated in principle by using either finite-difference or finite-element techniques. However, the choice is more restricted in the *two*-fluid situations and in our view the finite-element technique offers an appropriate method of tackling such problems, although the addition of body-fitted coordinates to our earlier algorithms could in principle lead us to the same capabilities. We therefore forsake the finite-difference techniques that were used with some success in parts 1 and 2 and concentrate on the more versatile finite-element method. The latter method has been developed in far greater depth in recent work in non-newtonian fluid mechanics (see, for example, Crochet & Walters 1983; Crochet *et al.* 1984) and this is a further motivation for our move from finite-difference to finite-element techniques.

Having confined attention to finite-element techniques, we must now acknowledge that the one used to simulate (successfully) the one-liquid situations for constant viscosity liquids has yet to be adapted for elastic liquids exhibiting variable viscosity behaviour. Accordingly, they cannot be used to simulate the behaviour of the P series polymer solutions.

Equations (7) or (9) have to be solved in conjunction with the familiar stress equations of motion, which in the absence of body forces, may be written in the form

$$-\nabla p+\nabla\cdot T=\rho\,\mathrm{D}\boldsymbol{v}/\mathrm{D}t, \tag{11}$$

where $\mathrm{D}/\mathrm{D}t$ represents the convected derivative. The velocity components must also satisfy the incompressibility constraint:

$$\nabla\cdot\boldsymbol{v}=0. \tag{12}$$

It is convenient to decompose the extra stress tensor in the following way (cf. Crochet *et al.* 1984). We write, for the Oldroyd B model,

$$T=T_1+T_2 \tag{13}$$

with

$$T_1+\lambda_1\overset{\nabla}{T}_1=2\eta_1 d, \tag{14}$$

$$T_2=2\eta_2 d, \tag{15}$$

From (9), (13)–(15), we have

$$\eta_1=\eta_0(\lambda_1-\lambda_2)/\lambda_1, \tag{16}$$

$$\eta_2=\eta_0\lambda_2/\lambda_1. \tag{17}$$

In the numerical simulations, we confine attention to $\lambda_2/\lambda_1=\frac{1}{9}$, this being the ratio usually used in simulations to exhibit the effect of viscoelasticity for a given λ_1 (see, for example, Crochet *et al.* 1984).

The boundary conditions to be associated with the governing equations depend upon the type of fluid model. We assume that the fluids do not slip along the solid boundaries and that the velocity field is imposed at entry sections. The extra stress components are also specified in the entry section for the part T_1 of T in (13). In an exit section, we impose a vanishing tangential velocity component, whereas the normal surface force component vanishes in the newtonian

case. The latter condition is invalid in the Oldroyd-B case because of the normal stresses; here, the normal velocity profile is imposed at an exit section.

The flow domain is covered by a mesh of finite elements; in the examples treated in the present paper we use isoparametric quadrilateral elements. In view of the implicit character of the constitutive equations (9) as opposed to the explicit equations (7), we use different discretization techniques for the newtonian and the Oldroyd B fluids. In the newtonian case, the velocity field $\boldsymbol{v}$ and the pressure field p are discretized in terms of nodal values $\boldsymbol{v}^i$, P^i and shape functions ψ_i, ϕ_i, respectively. We write

$$\tilde{\boldsymbol{v}} = \sum_{i=1}^{M} \boldsymbol{v}^i \psi_i, \quad \tilde{p} = \sum_{i=1}^{N} P^i \phi_i, \tag{18}$$

where M and N denote the number of nodes associated with the velocity and the pressure, respectively. The symbols $\tilde{\boldsymbol{v}}$ and $\tilde{p}$ stand for the finite-element approximation. For the velocity field, we use a continuous representation in terms of biquadratic lagrangian shape functions. In the examples dealing with a single fluid, we use a continuous representation for the pressure in terms of bilinear shape functions. (The case of two different fluids is discussed in §5ii.)

To obtain the values $\boldsymbol{v}^i$ and P^i, we apply the Galerkin method to the weak form of the stress equations of motion (11) and the incompressibility constraint (12), to give:

$$\int_\Omega \left[(\nabla \psi_i)^{\mathrm{T}} (-\tilde{p}\boldsymbol{I} + \tilde{\boldsymbol{T}}) + \psi_i \rho \frac{\mathrm{D}\tilde{\boldsymbol{v}}}{\mathrm{D}t} \right] \mathrm{d}\Omega = \int_{\partial\Omega} \psi_i \boldsymbol{t}, \tag{19}$$

$$\int_\Omega \phi_i \nabla \cdot \tilde{\boldsymbol{v}} \, \mathrm{d}\Omega = 0, \tag{20}$$

where $\boldsymbol{t}$ denotes the contact forces applied on the boundary $\partial\Omega$ of the flow domain Ω.

For the newtonian fluid, we substitute for $\boldsymbol{T}$ the expression

$$\tilde{\boldsymbol{T}} = \eta[\nabla\tilde{\boldsymbol{v}} + (\nabla\tilde{\boldsymbol{v}})^{\mathrm{T}}] \tag{21}$$

obtained on the basis of (7) and (18). The combination of (19), (20) and (21) provides an algebraic system of equations in terms of the nodal values $\boldsymbol{v}^i$ and P^i.

The substitution (21) is clearly impossible for the case of an elastic fluid of the differential type. We again use (18)–(20), but we must now substitute, in place of $\boldsymbol{T}$, the expression

$$\boldsymbol{T} = \eta_2[\nabla\boldsymbol{v} + (\nabla\boldsymbol{v})^{\mathrm{T}}] + \boldsymbol{T}_1, \tag{22}$$

and take note of the fact that $\boldsymbol{T}_1$ is given by an *implicit* constitutive equation. The problem may be solved by means of a mixed method in which the velocity field, the pressure and the extra stress tensor are all discretized in terms of nodal values (see, for example, Crochet *et al.* 1984). Thus, instead of (18), we write

$$\tilde{\boldsymbol{T}}_1 = \sum_{i=1}^{L} \boldsymbol{T}_1^i \pi_i, \quad \tilde{\boldsymbol{v}} = \sum_{i=1}^{M} \boldsymbol{v}^i \psi_i, \quad \tilde{p} = \sum_{i=1}^{N} P^i \phi_i, \tag{23}$$

where L denotes the number of nodes associated with the extra stress components, $\boldsymbol{T}_1^i$ are the nodal values and π_i the corresponding shape functions, the nature of which will be discussed below.

In order to calculate the T_1^i, we apply the Galerkin method to the constitutive equation, i.e.

$$\int_\Omega \pi_i\{\tilde{T}_1+\lambda_1\tilde{T}_1^{\nabla}-\eta_1(\nabla\tilde{v}+(\nabla\tilde{v})^{\mathrm{T}})\}\,\mathrm{d}\Omega=0. \tag{24}$$

The system (19)–(24) supplies the necessary number of algebraic equations to calculate the nodal values v^i, P^i and T_1^i.

Selecting the shape functions π_i, ψ_i and ϕ_i in (23) is a problem of major concern in simulating the flow of elastic liquids. In the applications related to the flow of two fluids with an interface, we use isoparametric quadrilateral elements in which the π_i and the ψ_i are both biquadratic lagrangian shape functions, whereas the ϕ_i are bilinear. It is well known, however, that viscoelastic problems are difficult to solve (see, for example, Crochet & Walters 1983; Crochet *et al.* 1984), one of the main reasons being the presence of important stress and velocity gradients near discontinuities in the boundary of the domain. In a recent paper, Marchal & Crochet (1986) have proposed a new set of shape functions, which now only apply to rectangular elements. The flow domains used in these experiments can be covered by a mesh of such elements, provided that it is not required to represent a curvilinear interface between two fluids by means of element boundaries. Accordingly, we restrict use of this powerful new element (which is called a hermitian element) to the *one*-fluid case.

The hermitian element is described in figure 16. For the velocity field, we use the velocity components and the velocity gradients at the corners as nodal values; thus, hermitian shape functions (HER 12) are used for the ψ_i. The shape functions π_i must be able to reproduce every gradient of the velocity vector $\tilde{v}$; in the present simulations we use bicubic lagrangian shape functions (LAG 16). Finally, the ϕ_i are bilinear and the representation $\tilde{p}$ for the pressure is continuous. The use of the hermitian mixed finite element has allowed us to extend appreciably the domain of convergence of our calculations, thus partly overcoming the high-Weissenberg-number problem that limited the scope of the simulations in parts 1 and 2 (see also Crochet *et al.* 1984).

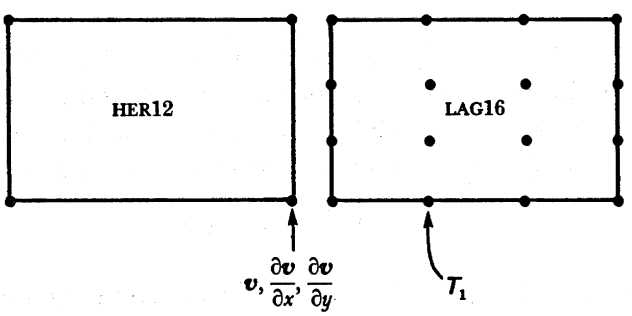

FIGURE 16. Hermitian finite element used for the viscoelastic calculations.

(ii) *Two liquids*

We now consider the plane stratified flow of two immiscible fluids. A typical situation is shown in figure 17. Fluids A and B enter the T geometry on the left- and right-hand sides, respectively, and are evacuated through the vertical branch. The fluids do not mix along the interface. The flow rates of A and B are known and we assume that the branches of the T are long enough so that we may impose fully developed velocity (and stress) profiles in the entry

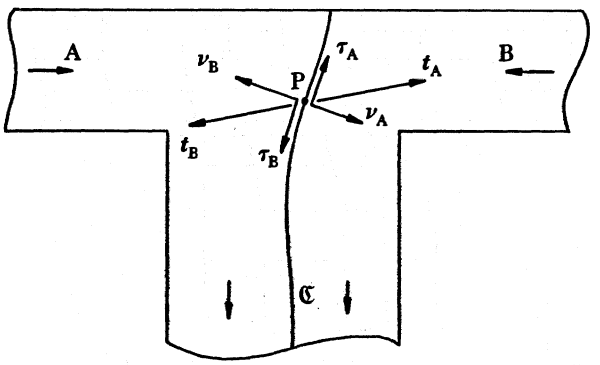

FIGURE 17. Typical geometry of stratified flow.

sections. The unknowns of the problem are the velocity fields in A and B and the location of the interface $\mathfrak{C}$.

Fluids A and B have specific material properties such as viscosities η_A and η_B and relaxation times λ_{1A} and λ_{1B}. The field and constitutive equations (11)–(15) apply to each fluid with the appropriate material constants. Additional conditions must be provided along the interface. At a point P of the interface $\mathfrak{C}$, let ν_A denote the external unit normal to the domain of fluid A, and let τ_A denote the unit tangent in the counterclockwise direction. Similarly, let ν_B and τ_B denote the corresponding vectors with respect to the domain covered by fluid B (figure 17). We have

$$\nu_A = -\nu_B, \quad \tau_A = -\tau_B. \tag{25}$$

Limiting attention to steady state flows, we require that neither A nor B flow through the interface, i.e.

$$\nu_A \cdot v_A = \nu_B \cdot v_B = 0, \tag{26}$$

the subscript A or B affixed to a variable denoting its association with either fluid A or fluid B.

We must also impose that the tangential velocity component is continuous across the interface $\mathfrak{C}$, i.e.

$$\tau_A \cdot v_A = -\tau_B \cdot v_B. \tag{27}$$

Let t_A and t_B denote the surface forces per unit area at point P acting upon fluids A and B, respectively. We have

$$t_A = (-p_A I + T_A)\,\nu_A, \quad t_B = (-p_B I + T_B)\,\nu_B. \tag{28}$$

In the absence of surface tension between A and B, we must have

$$t_A + t_B = 0. \tag{29}$$

We note that in view of (28), the continuity condition (29) for the surface forces does not necessarily require the continuity of the pressure p and of the components of the extra-stress tensors T_A and T_B.

We cover the flow domain by a finite-element mesh and we require that the interface coincides with element sides. A typical (coarse) mesh is shown in figure 18. Thus the interface is discretized by means of the nodes that lie upon it. The elements on the left of the interface are filled with fluid A, while those on the right are filled with fluid B. Assuming first that

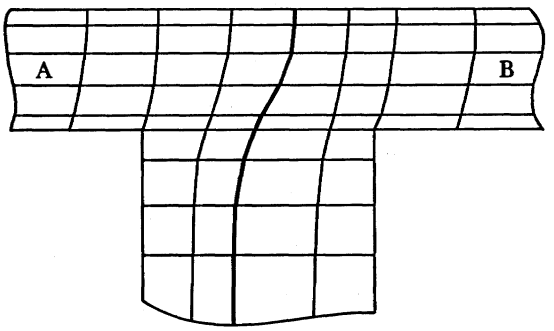

FIGURE 18. Typical (coarse) finite-element mesh for the geometry of figure 17.

the interface location is known, we describe the finite element equivalent of the conditions (26), (27) and (29).

Conditions (26) and (27) are easily implemented once a continuous velocity field is imposed across the mesh, i.e. the nodal velocity components on the interface are common to both fluids. Similarly, in the absence of surface tension, the continuity condition (29) is easily implemented by assuming equilibrium of the generalized nodal forces along the interface, as everywhere else in the mesh.

For completeness, we note that we need to take into account the fact that the pressure may be discontinuous across the interface. Furthermore, if a mixed method is used for calculating the flow of elastic liquids, it is necessary to provide for the possibility of discontinuous stress components across the interface. For the pressure, the problem is easily solved by selecting a discontinuous representation. Indeed, the weak form (19) of the stress equations of motion does not require that $\tilde{p}$ be continuous. Thus, the pressure is approximated by complete first-degree polynomials within each element, with discontinuities across the element boundaries. An additional advantage of such a representation for the pressure is a better approximation to the incompressibility constraint (12) because the number of discrete equations (20) is now higher than that for the case where $\tilde{p}$ is continuous.

A further possibility is to maintain a continuous representation but to assign *two* pressures at each node of the interface, i.e. one for fluid A and one for fluid B. The same procedure can be used for the extra stress components. However, it is inappropriate to elaborate any further on this point, because viscoelastic stratified flows will not be calculated in this paper.

We now need to describe briefly the method used for locating the interface. Earlier in this section, we assumed that the coordinates of the nodes on the interface are known, but in general this is not the case. The method used here is similar to the one proposed by Kistler & Scriven (1983). Consider in figure 19 a domain occupied by two fluids A and B separated by an interface $\mathfrak{C}$, and let P be a node on the interface. At the outset, we require that, while we search for the interface location, the node P will slide along the fixed line MN and be identified by its distance s from M. In figure 18, for example, the nodes of the interface move on horizontal lines and their location is identified by a horizontal coordinate. Thus, for each node of the interface, we need to calculate one scalar variable, and for that purpose we use the only equation which has not yet been implemented in our scheme, namely (26). Using an isoparametric representation of the interface, we find that the normal vector $\boldsymbol{v}$ depends upon the location of the nodes and we solve (26) in the mean. Details of this calculation will be presented elsewhere.

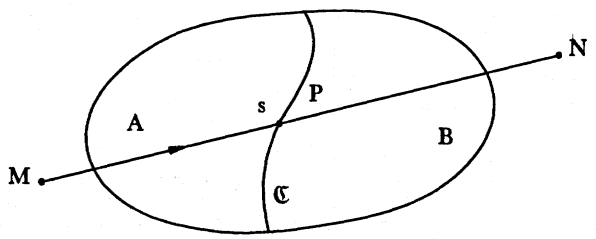

FIGURE 19. The motion of a point P on the interface is constrained to the straight line MN.

Finally, we need to solve a system of equations where the velocity components, the pressure and the location of the interface are the unknowns. The nonlinear set of equations is solved by means of Newton iterations, thus providing a quadratic rate of convergence.

6. NUMERICAL RESULTS

(i) *One liquid*

The situation in the T geometry when there is only one feeder arm is considered in figures 20 and 21. From figure 5*a* we determined the flow rates in the exit arms and we imposed these as boundary conditions for both the newtonian and the viscoelastic cases. The viscoelastic results were obtained by increasing progressively the value of the relaxation time of the Oldroyd B fluid, maintaining the ratio of λ_2/λ_1 as $\frac{1}{8}$. The maximum value of λ_1 that was attainable was 0.1 s.

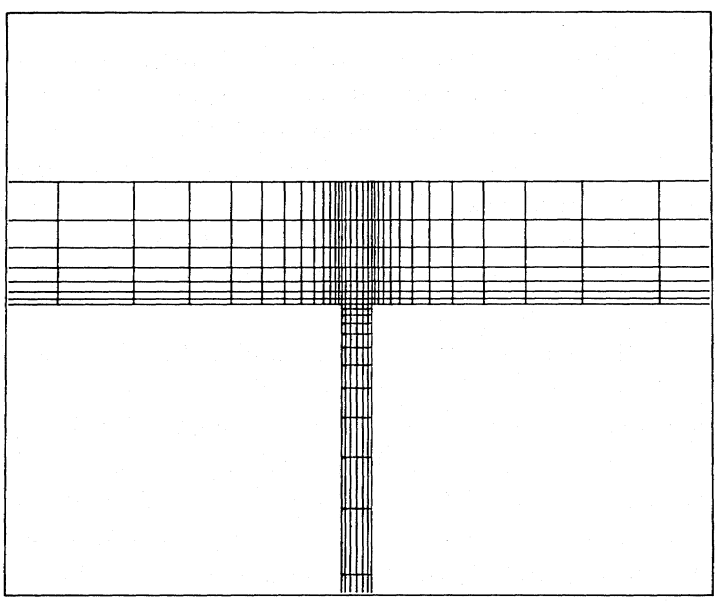

FIGURE 20. Central region of finite-element mesh for calculating the flow of one liquid in a T geometry.

We used the hermitian elements with the mesh shown in figure 20, which contains 328 elements and 1425 nodes; the system contains approximately 5000 unknowns. Figure 21 compares the streamlines for the newtonian and the elastic liquid situations, the latter corresponding to a value of $W = 0.044$ in the entry section. It is clear that, qualitatively at

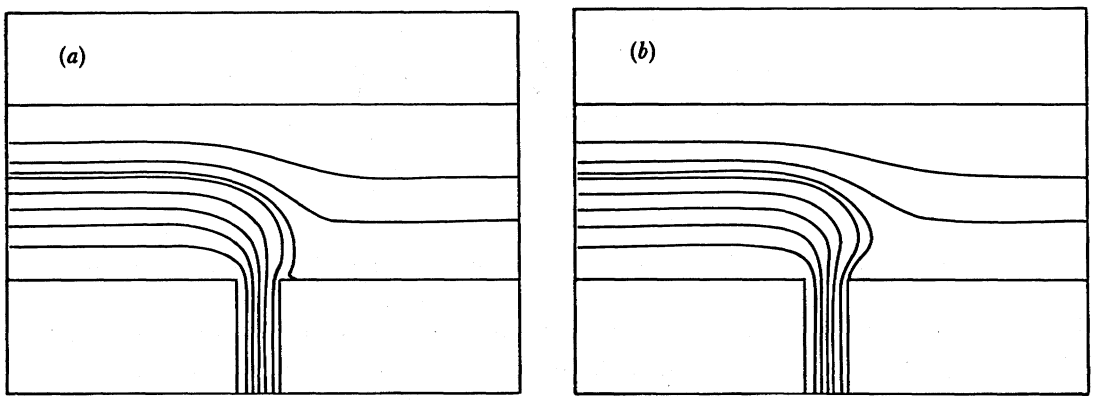

FIGURE 21. Numerical simulation of flow in a T geometry with fluid entering at A and exiting at B and C. (*a*) Conditions relevant to figure 5*a* with $R = 0.054$, $W = 0$ at entry. (*b*) Same conditions as for (*a*) except $W = 0.044$.

least, the numerical simulation shows the same tendency as the experimental results, i.e. a characteristic overshoot of the dividing streamline in the case of the elastic liquid. However, the simulations are completely inadequate to predict a gross overshoot of the sort shown in figure 5*b*. This is another example of the inadequacy of present numerical simulations to predict *quantitatively* the behaviour of elastic liquids when *extreme* viscoelastic effects are in evidence. This deficiency is not a reflection of the numerical method used. It rather points to the inadequacies of the simple fluid models that are currently in use. Resolving this problem may be a major undertaking.

We now confine attention to the situation in which fluid enters two arms of the T geometry. The conditions encountered in the newtonian fluid experiments of figure 6 have been faithfully reproduced in the numerical simulations given in figure 22. The agreement between experiment and theory is excellent. In particular, the shape of the weak recirculating vortex in figure 22*a* is in very good agreement with the experimental features demonstrated in figure 6*b*, and we note with interest that it was the availability of the well-defined vortex structure in the numerical simulation of figure 22*a* that motivated a detailed study of the precise form of the weak vortex in the experiments (cf. §4i).

Early attempts to predict the distinctive features exhibited in the case when elastic liquids flow in the T geomety were unproductive. The use of the finite-difference techniques of parts 1 and 2 and also the then available finite-element techniques failed to predict any vortex activity. However, the use of the new hermitian elements, which were successfully used by Marchal & Crochet (1986) to simulate contraction flows, has significantly advanced our understanding of viscoelastic flow in a T geometry. This new development has allowed numerical simulations to be performed at (and beyond) the conditions encountered in the experiments. Figure 23 contains numerical simulations for a typical set of conditions, figure 23*b* representing conditions just before the numerical algorithm broke down. The appearance of two lip vortices is evident with the larger vortex associated with the slower moving stream. This is in *qualitative* agreement with the experimental results discussed in §4i. However, when the simulations are compared with available experimental results as in figure 23*a* we see that there is no *quantitative* agreement. There is therefore encouragement that important flow features are now being simulated for the first time, but discouragement that quantitative agreement

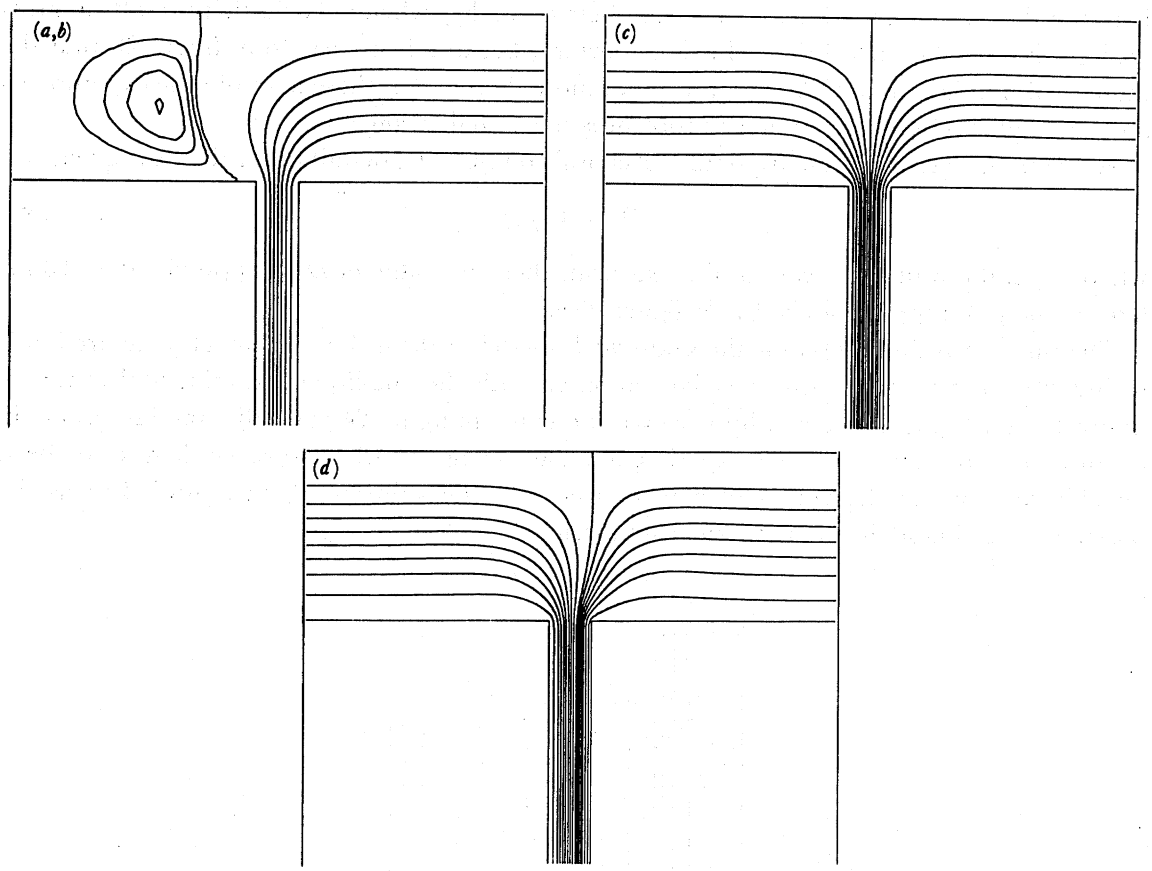

FIGURE 22. Numerical simulation of newtonian flow in a T geometry with (N4) fluid entering arms A and B. (*a*) $R_A = 0$, $R_B = 0.058$, total flow rate is 3.0 ml s^{-1}; (*b*) $R_A = 0$, $R_B = 0.058$, total flow rate is 3.0 ml s^{-1}; (*c*) $R_A = 0.058$, $R_B = 0.058$, total flow rate is 6.0 ml s^{-1}; (*d*) $R_A = 0.065$, $R_B = 0.028$, total flow rate is 4.8 ml s^{-1}.

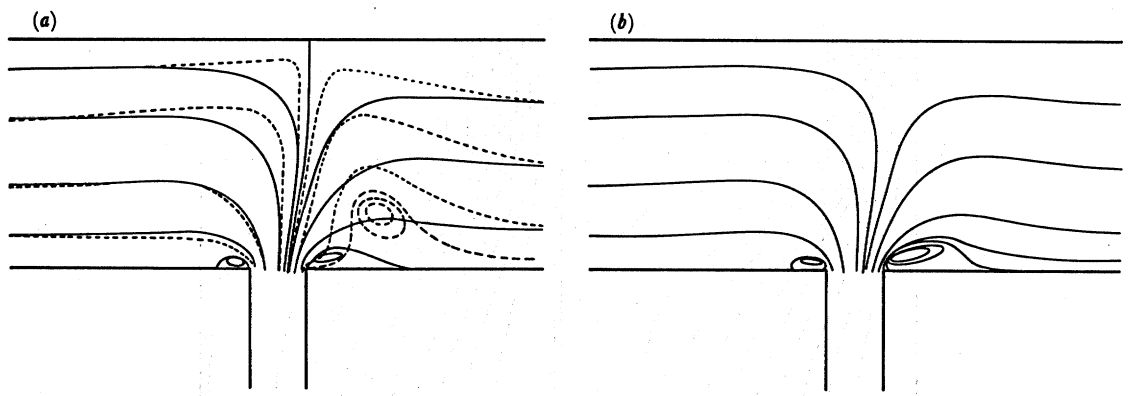

FIGURE 23. Numerical simulation for an elastic liquid in the T geometry. (*a*) full line-numerical simulation for B45 (with $\lambda_2/\lambda_1 = \frac{1}{9}$). The broken line represents streamlines determined from an experimental photograph. $R_A = 0.7$, $R_B = 0.3$, $W_A = 0.068$, $W_B = 0.03$. (*b*) Numerical simulation for B45 (with $\lambda_2/\lambda_1 = \frac{1}{9}$). $R_A = 0.875$, $R_B = 0.375$, $W_A = 0.085$, $W_B = 0.0375$.

between theory and experiment is far from being a reality when viscoelasticity results in gross changes in flow characteristics. This is important, because it is clear from figure 23 that the numerical simulations are for conditions that more than match those found in the experiments and the high Weissenberg number problem is not a major concern.

We remark that, if we use a popular Deborah number D_e definition of the flow given by

$$D_e = \lambda_1 \gamma_w, \tag{30}$$

where γ_w is the wall shear rate in the exit arm, then the value of D_e is approximately 10 for figure 23*a* and approximately 12 for figure 23*b*.

The numerical simulation for the Oldroyd B model in the 4:1 step geometry (figure 3*c*) is included in figure 24 and this may be compared with the one-liquid experimental results of figure 12. The appearance of a lip vortex is indicated in figure 24*c* and the simulations are in favourable agreement with the experimental data of figure 12*c*. However, it has not been possible to simulate the vortex seen in figure 12*d*. The value of D_e in figure 24*c* was the maximum attainable in the numerical simulations.

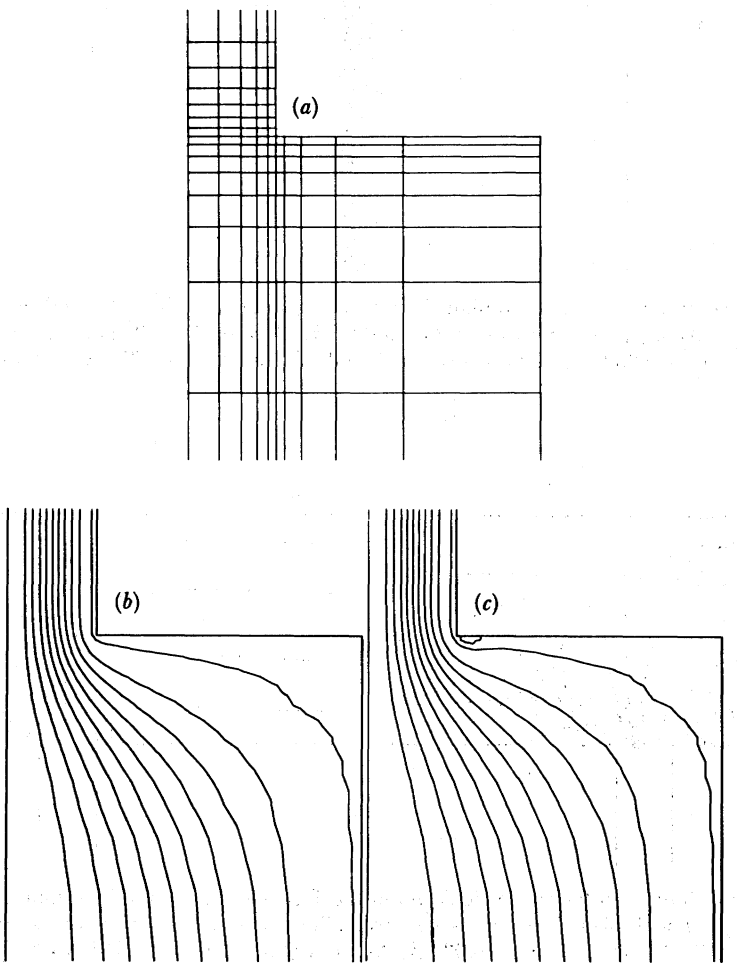

FIGURE 24. Numerical simulation for an elastic liquid in the planar step geometry (3). (*a*) Expanded view of the mesh near the reentrant corner; (*b*) newtonian $R = 0.058$, $W = 0$; (*c*) B49, $R = 0.062$, $W = 0.025$ corresponding to $D_e = 9.6$.

(ii) *Two liquids*

Here, we attempt to simulate the two-(newtonian) liquid flow in the T geometry demonstrated in figure 10. To facilitate this, we make use of the techniques developed in §5ii. The interface is not known *a priori* and is calculated by means of the Newton–Raphson algorithm.

The initial mesh is shown in figure 25. The nodes will move horizontally depending on the location of the interface.

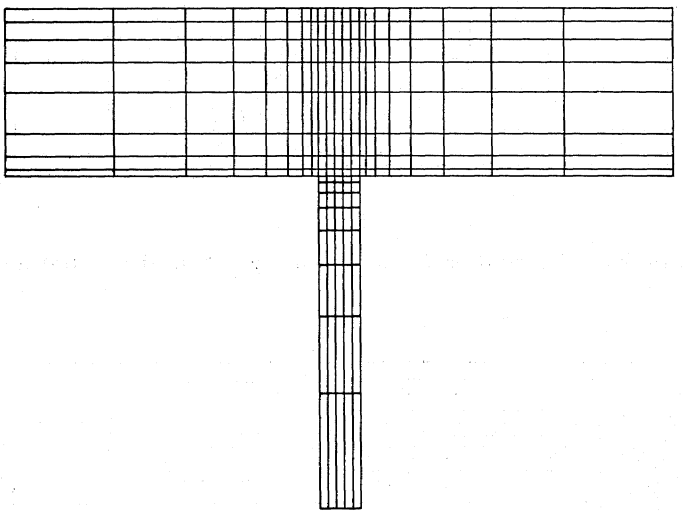

FIGURE 25. Initial finite-element mesh for the two-fluid situation.

A slight problem was encountered at the contact point between the interface and the upper wall near the stagnation point. Indeed, near the stagnation point, (26) is essentially trivially satisfied and one obtains an indeterminacy for the location of the attachment point. In the present paper we have imposed an angle of contact $\frac{1}{2}\pi$ between the wall and the interface. Several other strategies have also been used in the course of the numerical developments. However, they all lead to the same streamlines in the global flow, although some of them produce important distortions of the elements near the wall.

Figure 26*a–c* shows the final deformed meshes corresponding to the flows demonstrated in figure 27 *a–c* respectively. The streamlines in figure 27 may be compared with the corresponding experimental photographs shown in figure 10. The agreement between numerical simulation and experiment is excellent. Particularly gratifying is the agreement between figure 10*c* and figure 27*c*.

It has been possible to adapt the two-liquids strategy to cover elastic liquids. However, this has necessarily involved the use of conventional finite elements (rather than the rectangular hermitian elements) and the resulting simulations have not been able to reach or reproduce the conditions and dramatic experimental results shown in figures 11, 13–15 (and are not therefore included in this paper). This lack of utility is not surprising, because the use of such elements cannot even predict satisfactorily the *one*-liquid characteristics. Successful exploitation of the strategy discussed in §5ii to the two-(elastic) liquid situation must therefore await the availability of new isoparametric elements.

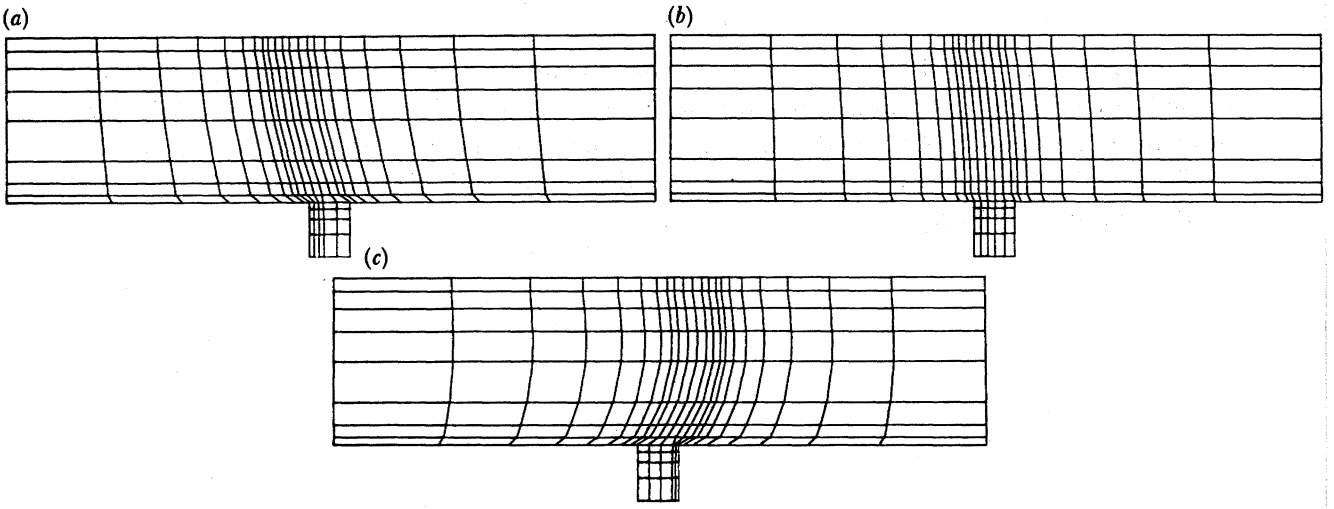

FIGURE 26. Final deformed meshes corresponding to flows demonstrated in figure 27.

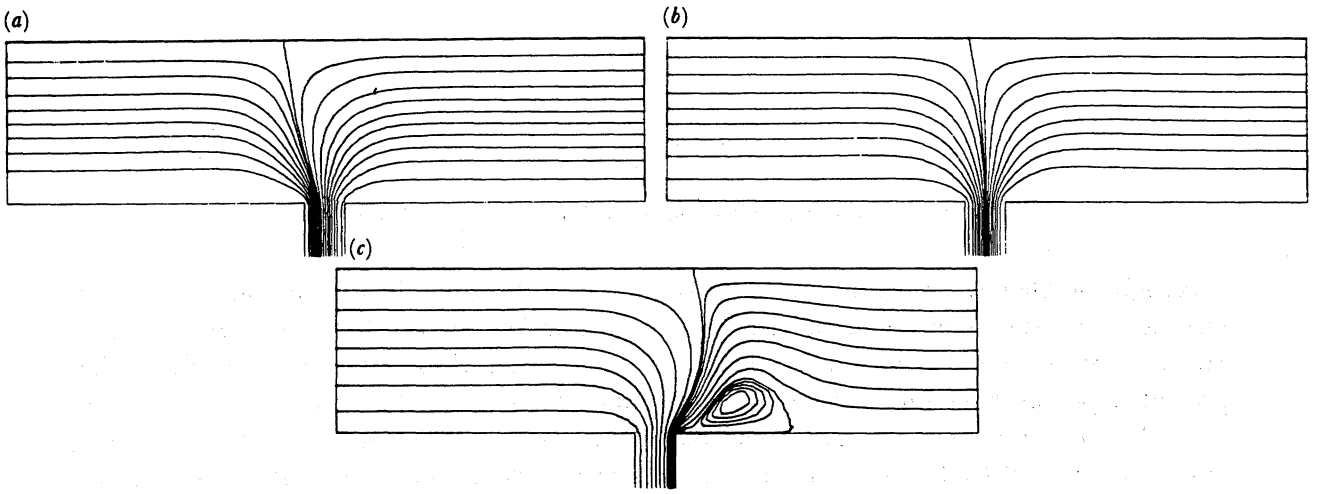

FIGURE 27. Numerical simulation for two newtonian fluids N10 and N11 in the T geometry (3*a*) (cf. figure 10). (*a*) $R_A = 0.09$, $R_B = 0.41$, total flow rate is 18 ml s^{-1}; (*b*) $R_A = 0.14$, $R_B = 0.26$, total flow rate is 15.4 ml s^{-1}; (*c*) $R_A = 0.12$, $R_B = 0.02$, total flow rate is 6.54 ml s^{-1}.

7. CONCLUSIONS

For completeness we summarize the main conclusions reached in this paper.

(i) When elastic liquids flow in a T geometry, substantial lip vortices appear that are not present in the case of newtonian liquids. For constant viscosity Boger liquids, the lip vortices essentially disappear when the flow rates in the two entry arms are balanced. This is not the case for the shear thinning P polymer solutions.

(ii) When two liquids are used in the experiments, one being newtonian and the other highly elastic, the flow in the newtonian liquid can resemble that in a highly elastic liquid. We associate this dramatic behaviour with the strong flow condition along the interface between the two liquids.

(iii) Finite-element techniques with new hermitian elements are able to simulate qualitatively the flow characteristics found for elastic liquids in the T and step geometries. There is no quantitative agreement and the present work adds further weight to the need for a detailed reappraisal of the use of simple constitutive models in the simulation of flows where viscoelasticity results in gross changes in flow characteristics.

(iv) The finite-element simulation of the flow of one or two newtonian liquids is excellent. The application of the strategies used in the present paper to the flow of two elastic liquids must await the development of new isoparametric elements.

We express indebtedness to Dr J. M. Marchal for significant assistance in the numerical simulation aspects of the present work and Mr R. E. Evans for equally invaluable assistance in experimental aspects of the work. D. M. B. was financed by a Research Grant from the S.E.R.C.

References

Boger, D. V. 1977/78 *J. Non-Newtonian Fluid Mech.* **3**, 87–91.
Boger, D. V., Hur, D. U. & Binnington, R. J. 1986 *J. Non-Newtonian Fluid Mech.* **20**, 31–49.
Choplin, L., Carreau, P. J. & Ait Kadi, A. 1983 *Polym. Engng Sci.* **23**, 459–464.
Cochrane, T., Walters, K. & Webster, M. F. 1981 *Phil. Trans. R. Soc. Lond.* A **301**, 163–181.
Crochet, M. J., Davies, A. R. & Walters, K. 1984 *Numerical simulation of non-newtonian flow.* New York and Amsterdam: Elsevier.
Crochet, M. J. & Walters, K. 1983 *A. Rev. Fluid Mech.* **15**, 241–260.
Evans, R. E. & Walters, K. 1986 *J. Non-Newtonian Fluid Mech.* **20**, 11–29.
Jackson, K. P., Walters, K. & Williams, R. W. 1984 *J. Non-Newtonian Fluid Mech.* **14**, 173–188.
Keentok, M., Georgescu, A. G., Sherwood, A. A. & Tanner, R. I. 1980 *J. Non-Newtonian Fluid Mech.* **6**, 303–324.
Kistler, S. F. & Scriven, L. E. 1983 In *Computational analysis of polymer processing* (ed. J. R. A. Pearson & S. M. Richardson), pp. 243–299. Barking, Essex: Applied Science Publishers.
Marchal, J. M. & Crochet, M. J. 1986 *J. Non-Newtonian Fluid Mech.* **20**, 187–207.
Metzner, A. B., Uebler, E. A. & Chan Man Fong, C. F. 1969 *Am. Inst. chem. Engng J.* **15**, 750–758.
Oldroyd, J. G. 1950 *Proc. R. Soc. Lond.* A **200**, 523–541.
Walters, K. 1975 *Rheometry.* London: Chapman and Hall.
Walters, K. & Webster, M. F. 1982 *Phil. Trans. R. Soc. Lond.* A **308**, 199–218.

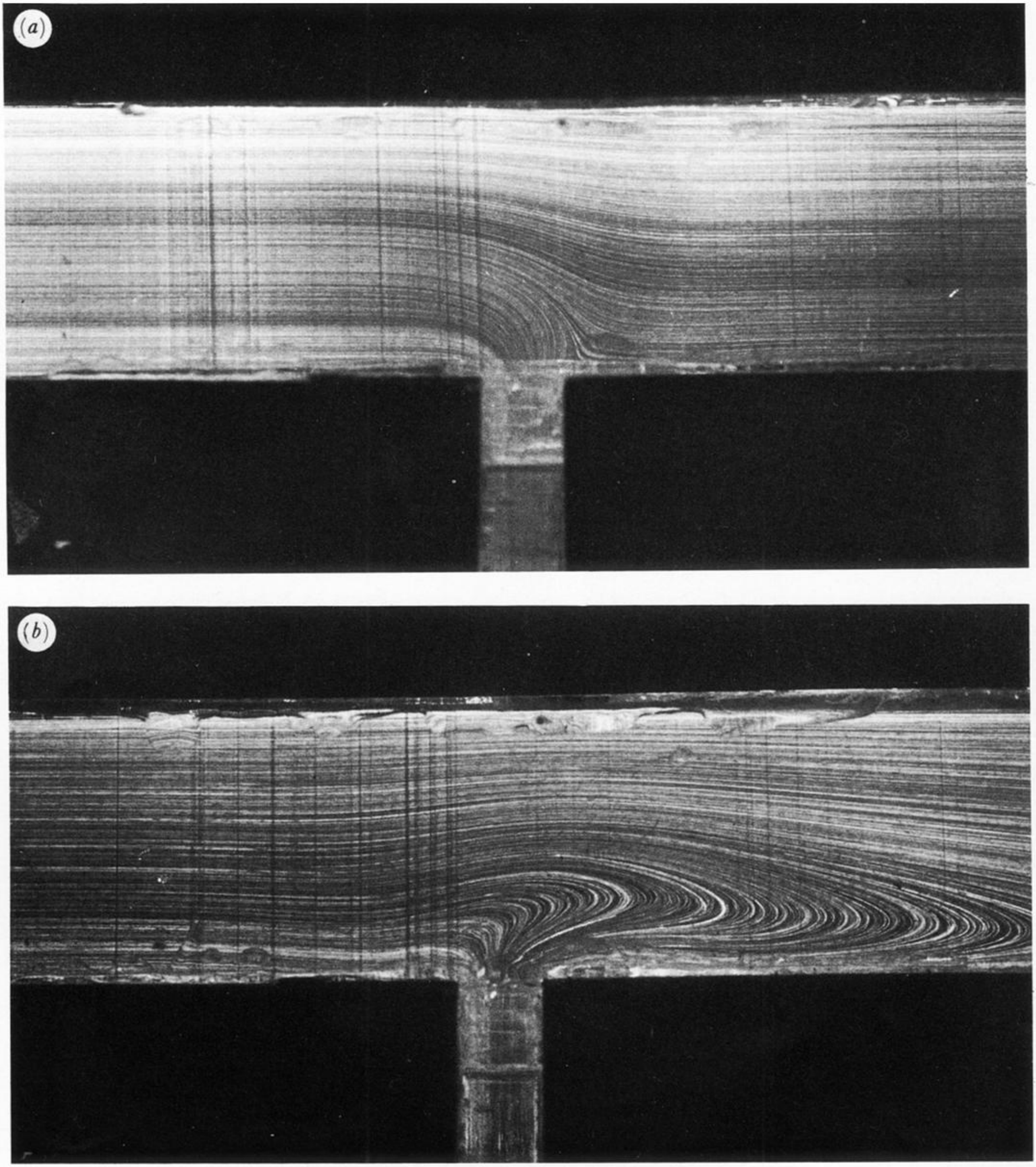

FIGURE 5. T geometry (3*a*) with one fluid. Fluid enters at A and exits at B and C. The R and W numbers are based on inlet conditions. (*a*) Fluid N9, $R = 0.054$, $W = 0.0$; (*b*) fluid B49: $R = 0.071$, $W = 0.29$.

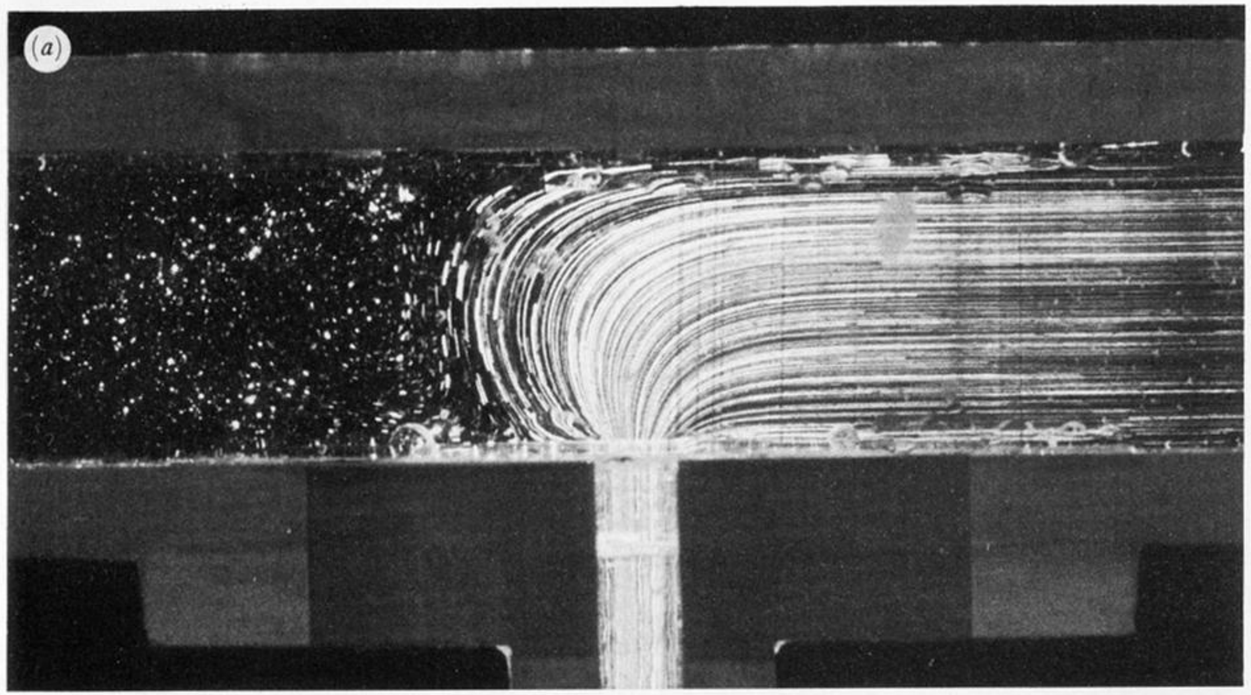

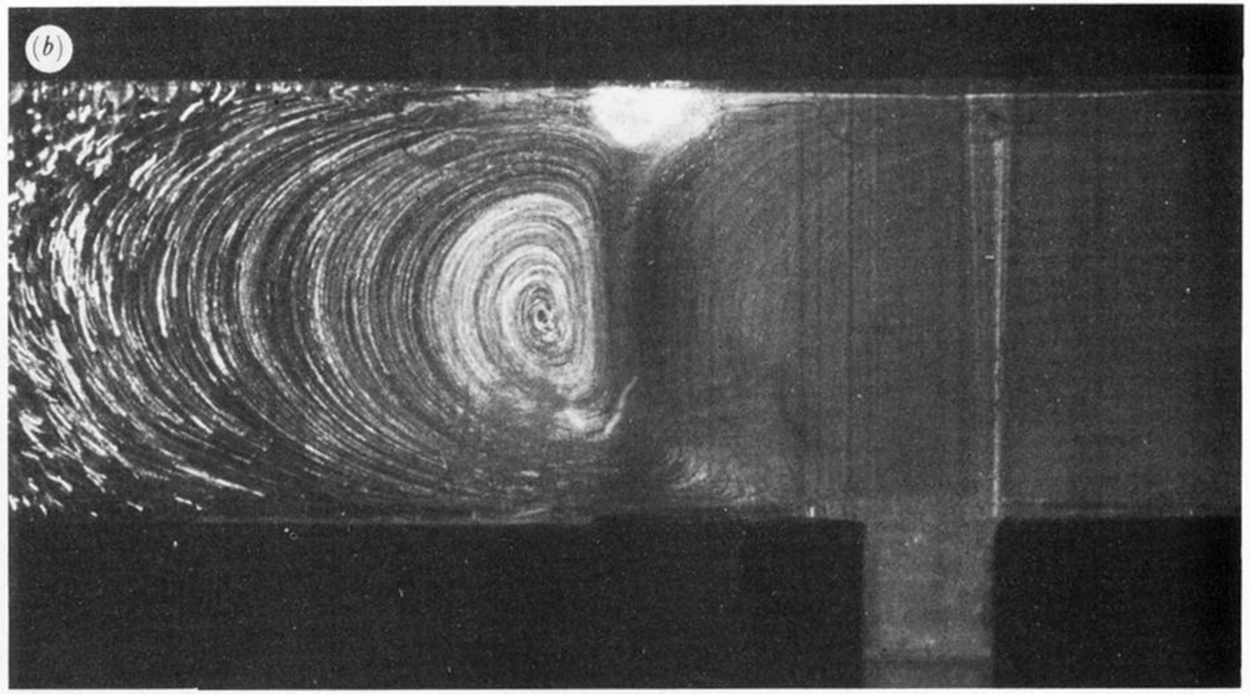

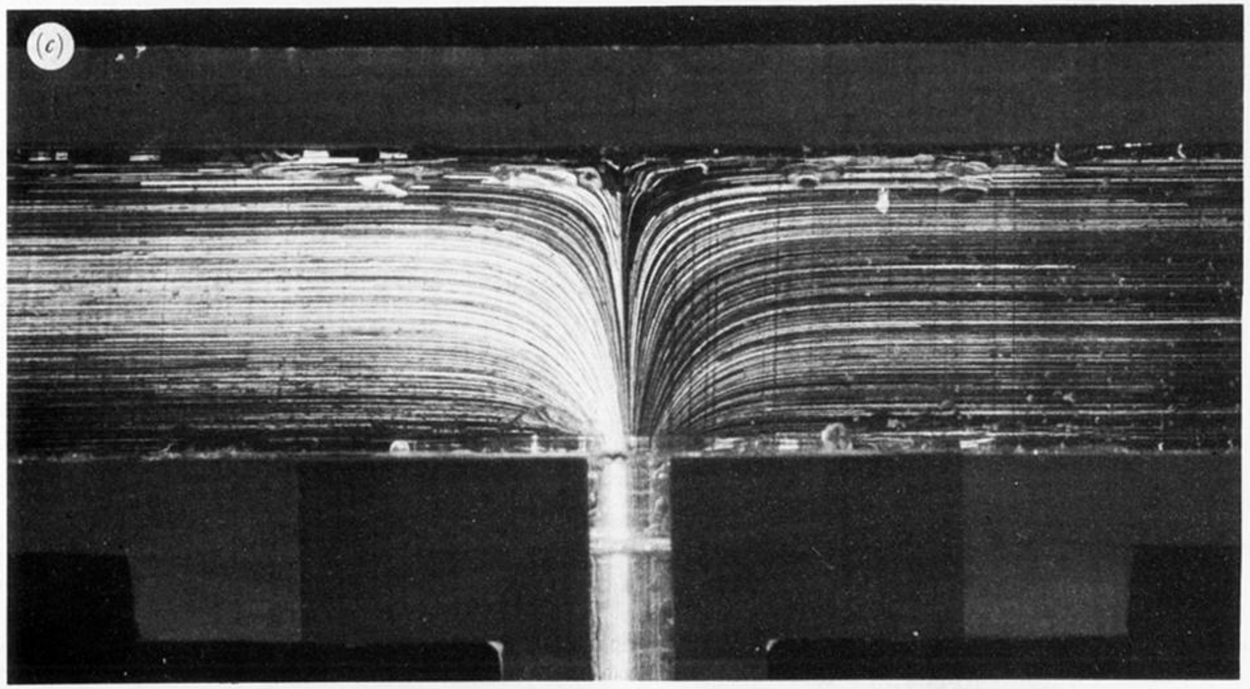

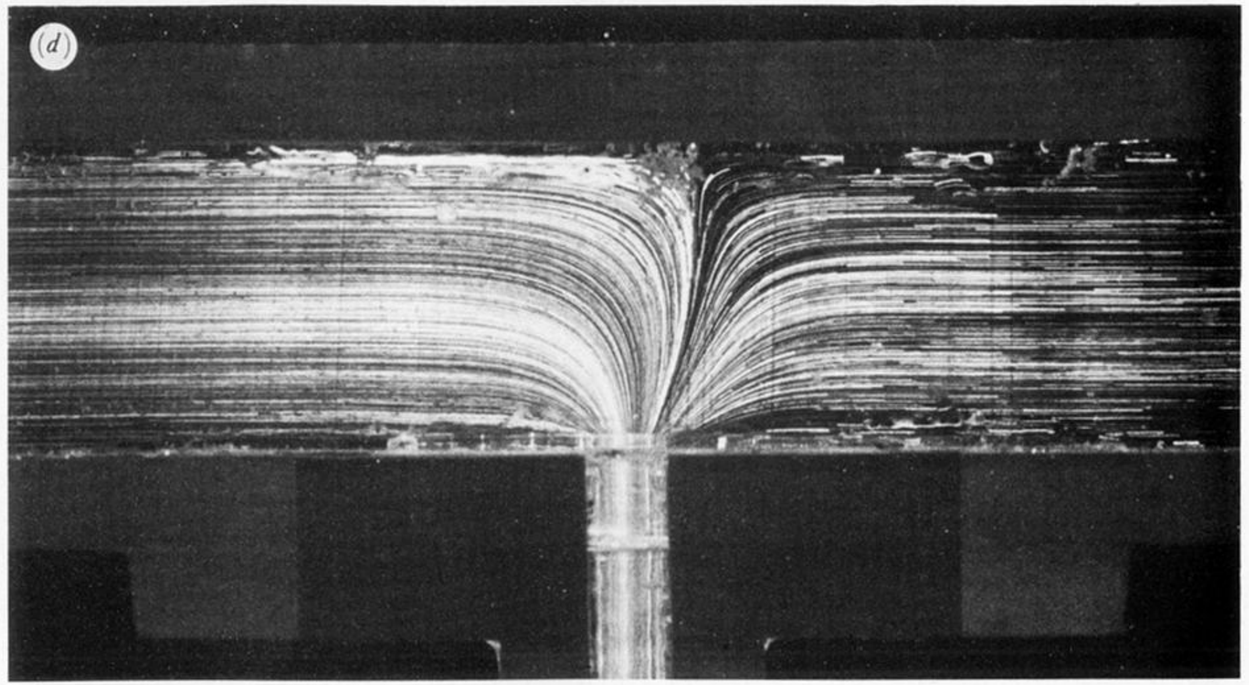

FIGURE 6. T geometry (3*a*) with newtonian fluid N4 entering through arms A and B. (*a*) $R_A = 0$, $R_B = 0.058$, total flow rate is 3.0 ml s^{-1}; (*b*) $R_A = 0$, $R_B = 0.058$, total flow rate is 3.0 ml s^{-1}; (*c*) $R_A = 0.058$, $R_B = 0.058$, total flow rate is 6.0 ml s^{-1}; (*d*) $R_A = 0.065$, $R_B = 0.028$, total flow rate is 4.8 ml s^{-1}.

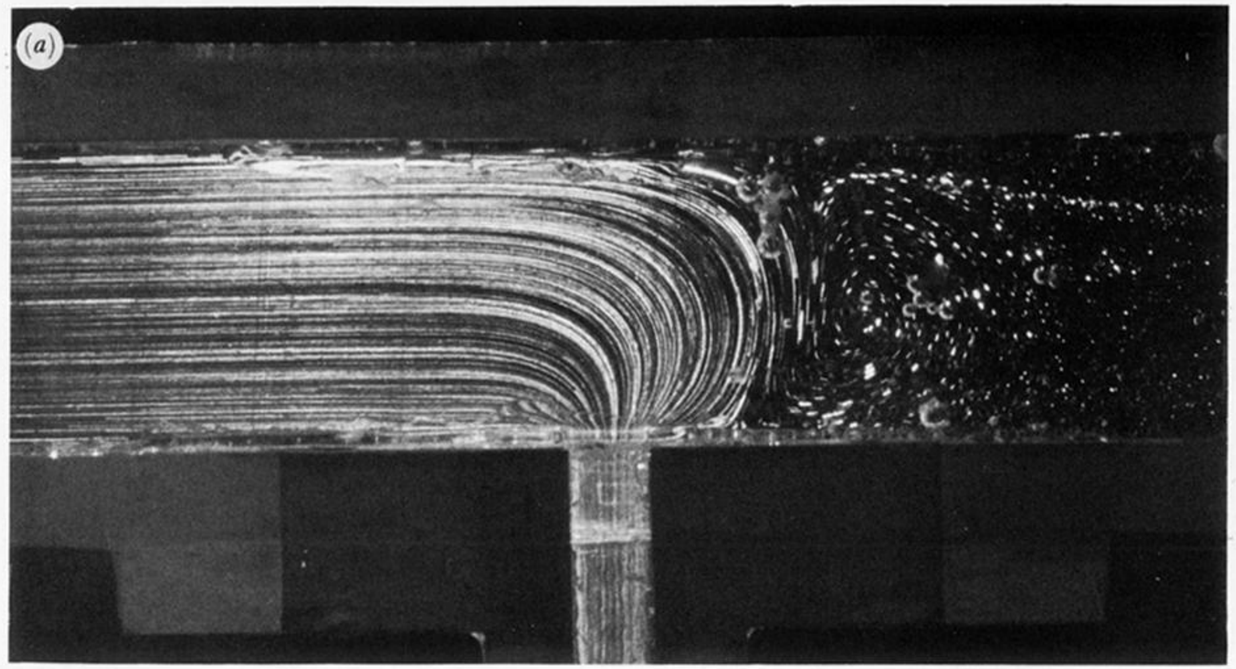

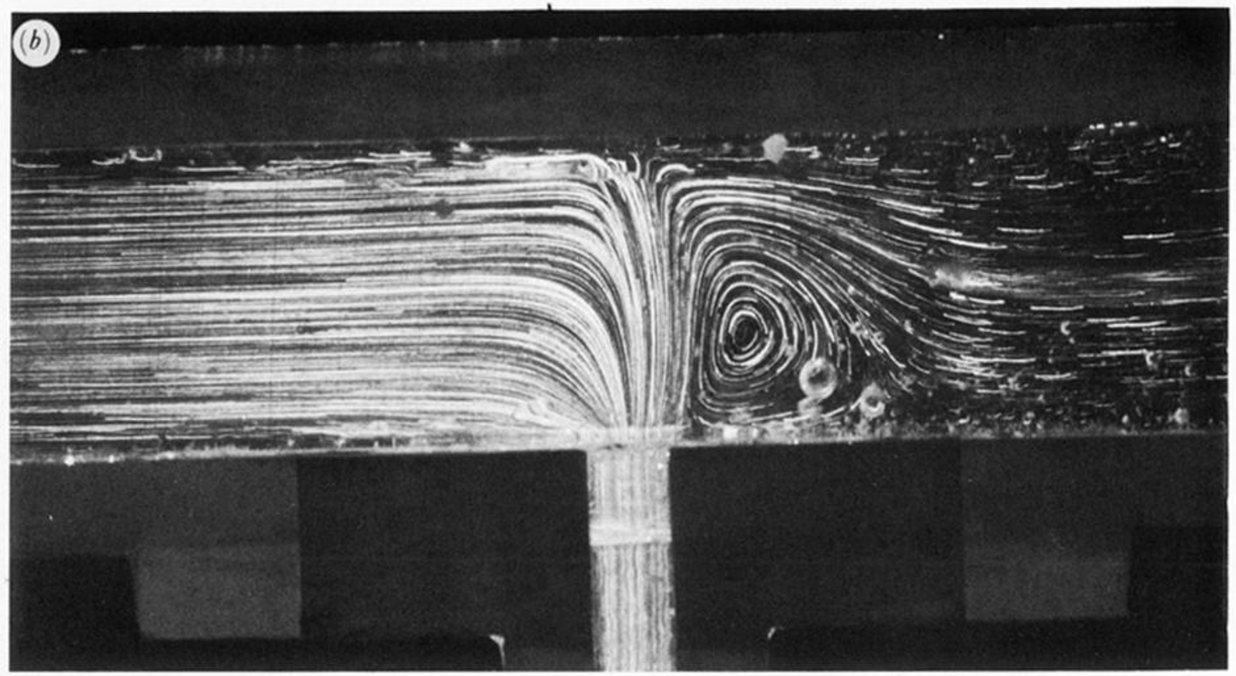

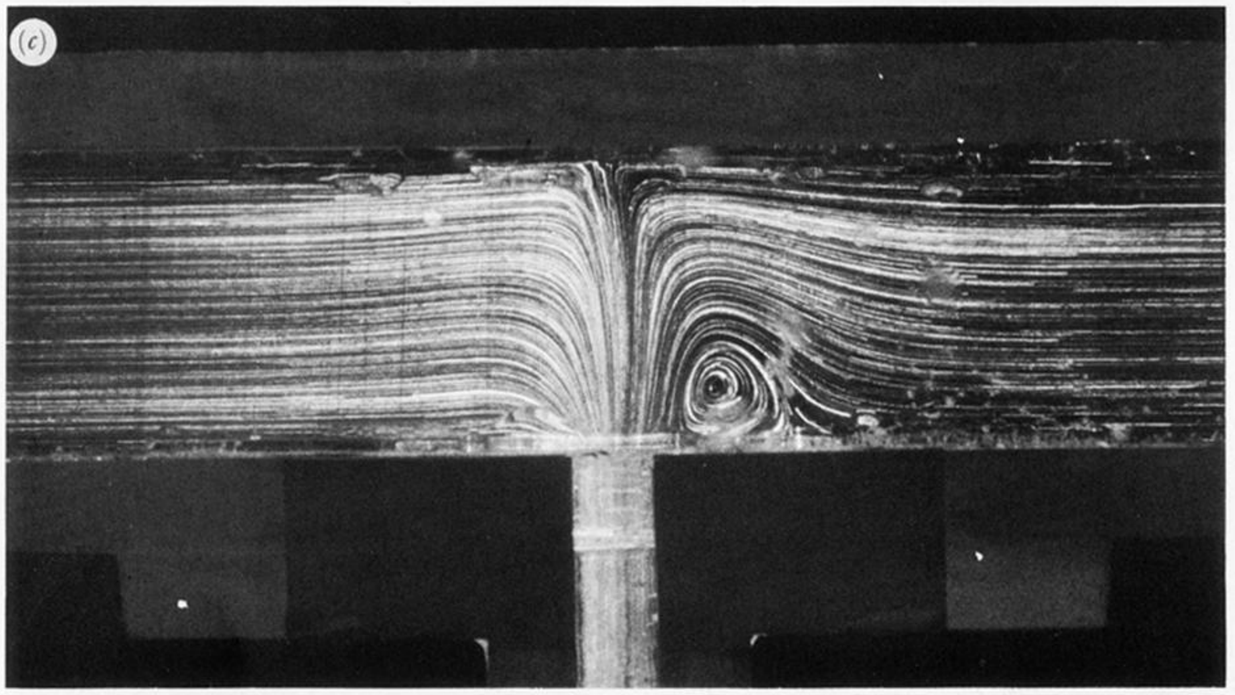

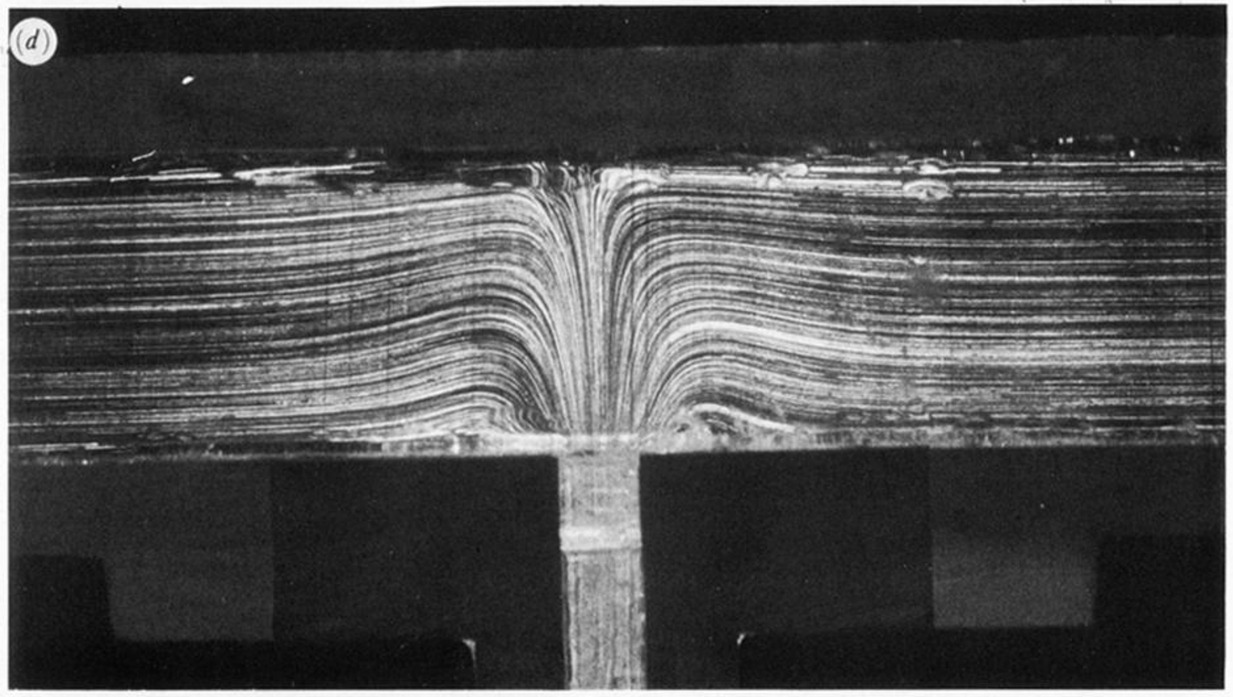

FIGURE 7. T geometry (3*a*) with Boger fluid B44 entering through arms A and B. (*a*) $R_A = 0.16$, $R_B = 0$, $W_A = 0.055$, $W_B = 0$, total flow rate is 1.6 ml s^{-1}; (*b*) $R_A = 0.016$, $R_B = 0.004$, $W_A = 0.053$, $W_B = 0.013$, total flow rate is 1.95 ml s^{-1}; (*c*) $R_A = 0.012$, $R_B = 0.008$, $W_A = 0.04$, $W_B = 0.026$, total flow rate is 1.95 ml s^{-1}; (*d*) $R_A = 0.014$, $R_B = 0.014$, $W_A = 0.048$, $W_B = 0.048$, total flow rate is 2.8 ml s^{-1}.

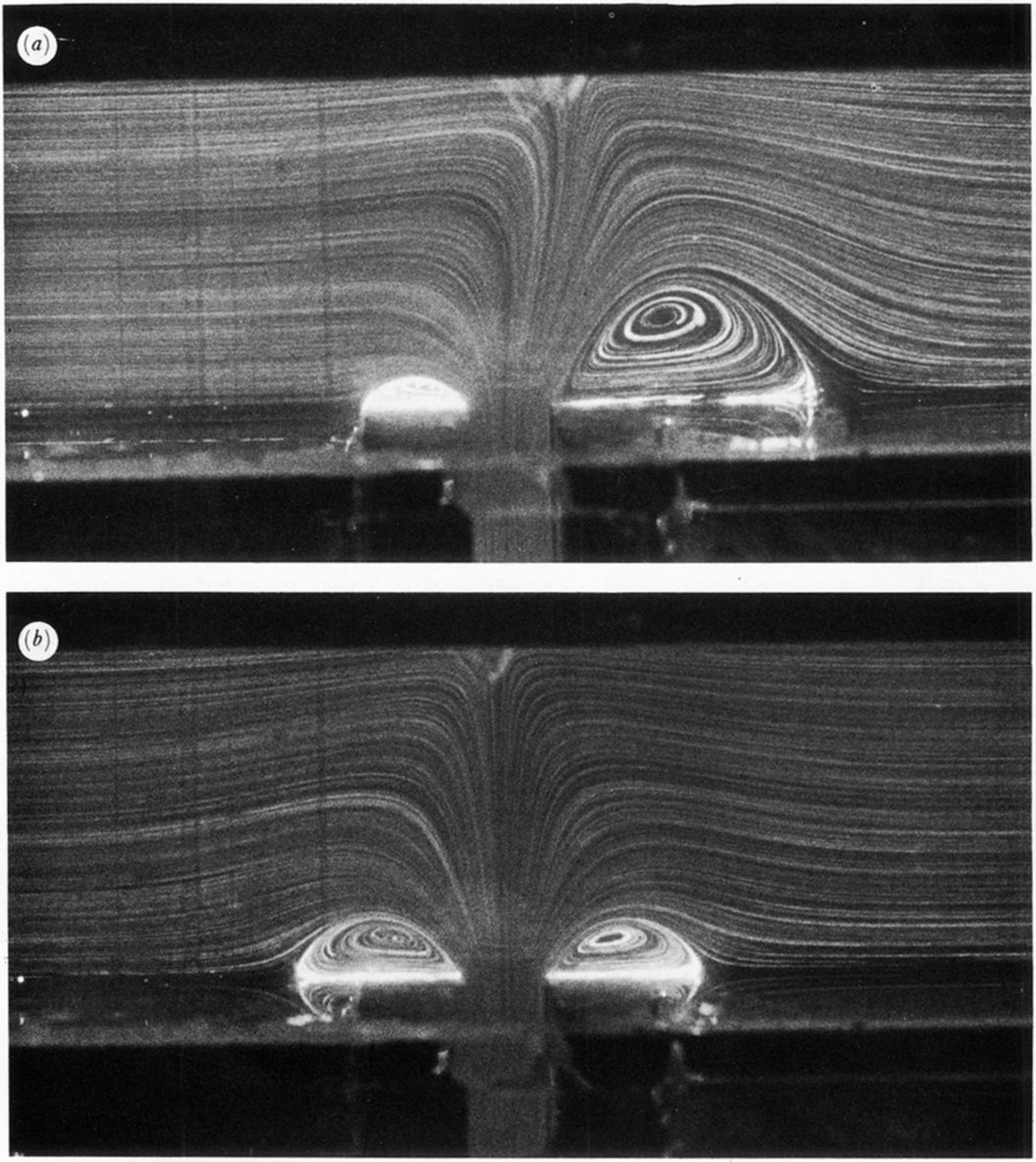

FIGURE 8. T geometry (3*b*) with shear thinning fluid P entering through arms A and B. (*a*) $Q_A = 49.1$ ml s^{-1}, $Q_B = 22.3$ ml s^{-1}; (*b*) $Q_A = Q_B = 35.7$ ml s^{-1}.

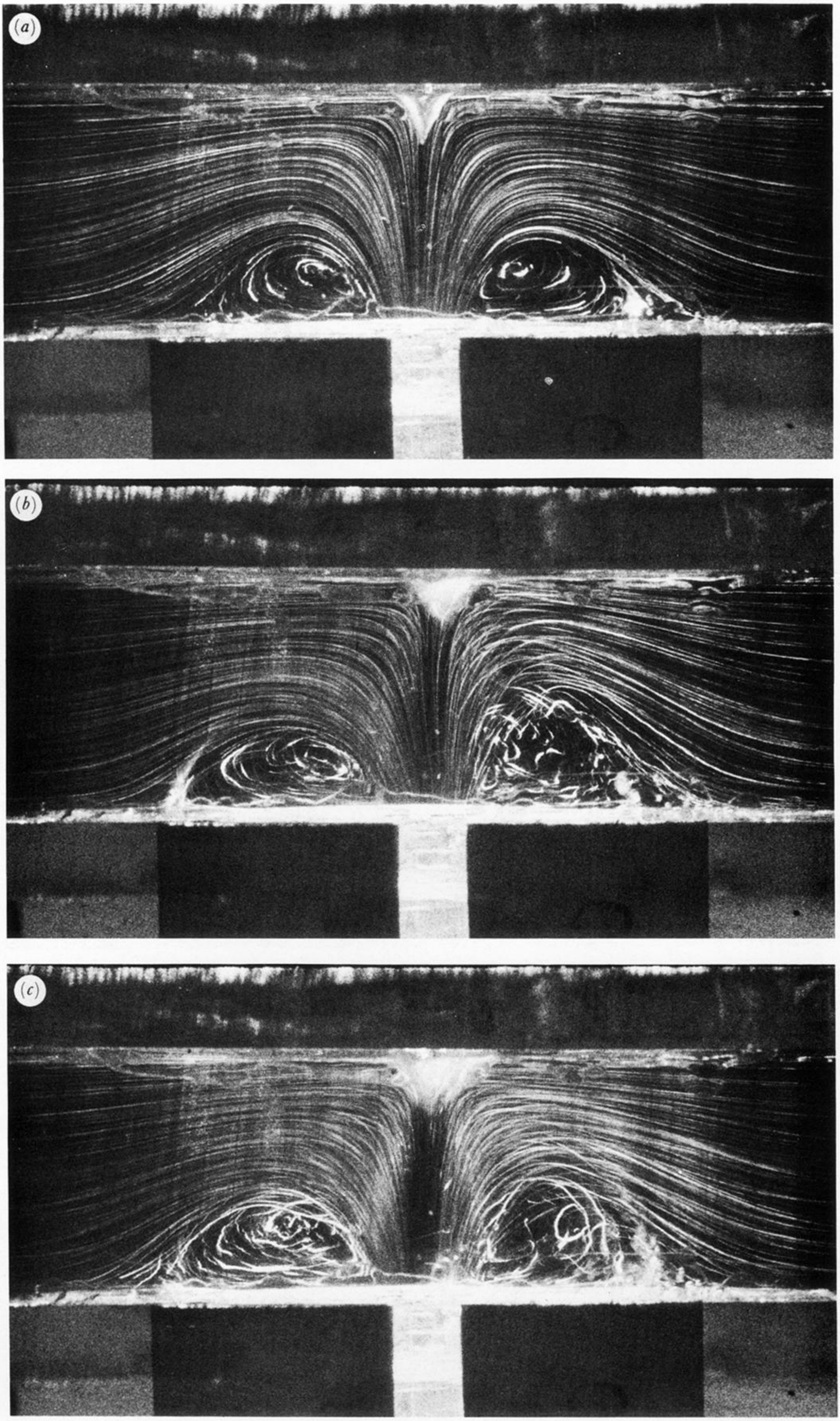

FIGURE 9. T geometry (3*a*) with shear thinning fluid P entering through arms A and B. (*a*) $Q_A = Q_B = 5.2$ ml s^{-1}; (*b*) $Q_A = Q_B = 7.5$ ml s^{-1}; (*c*) $Q_A = Q_B = 10.0$ ml s^{-1}.

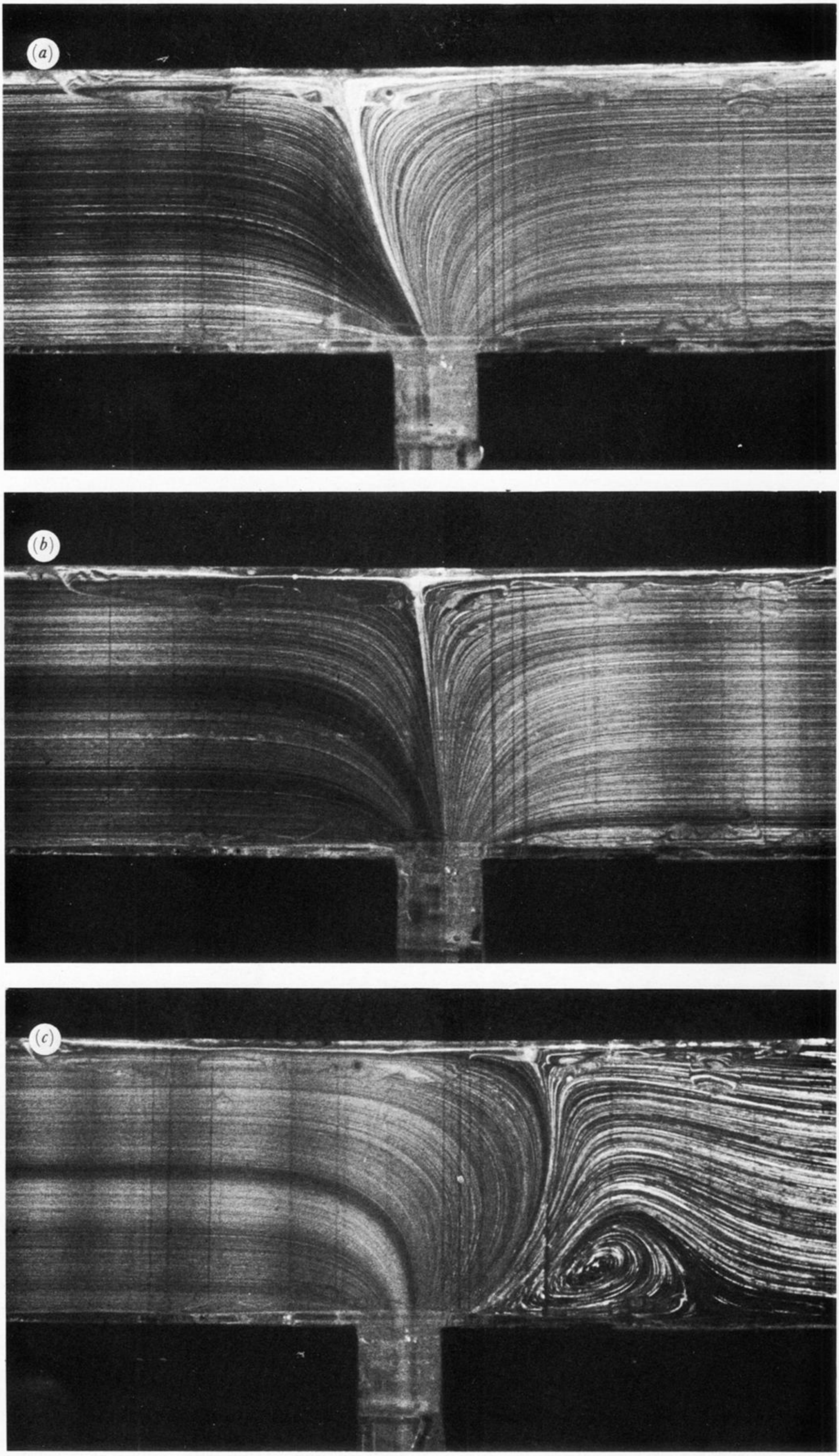

FIGURE 10. T geometry (3*a*) with newtonian fluids N10 and N11 entering through arms A and B, respectively. (*a*) $R_A = 0.09$, $R_B = 0.41$, total flow rate is 18 ml s^{-1}; (*b*) $R_A = 0.14$, $R_B = 0.26$, total flow rate is 15.4 ml s^{-1}; (*c*) $R_A = 0.12$, $R_B = 0.02$, total flow rate is 6.45 ml s^{-1}.

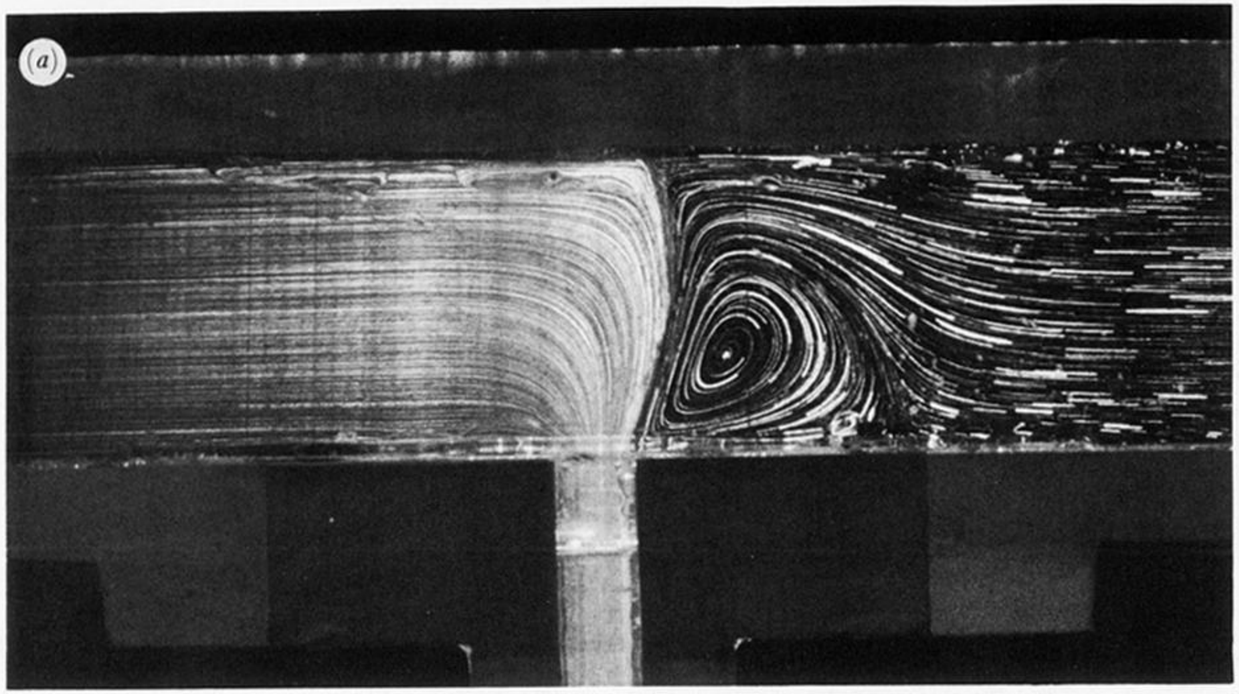

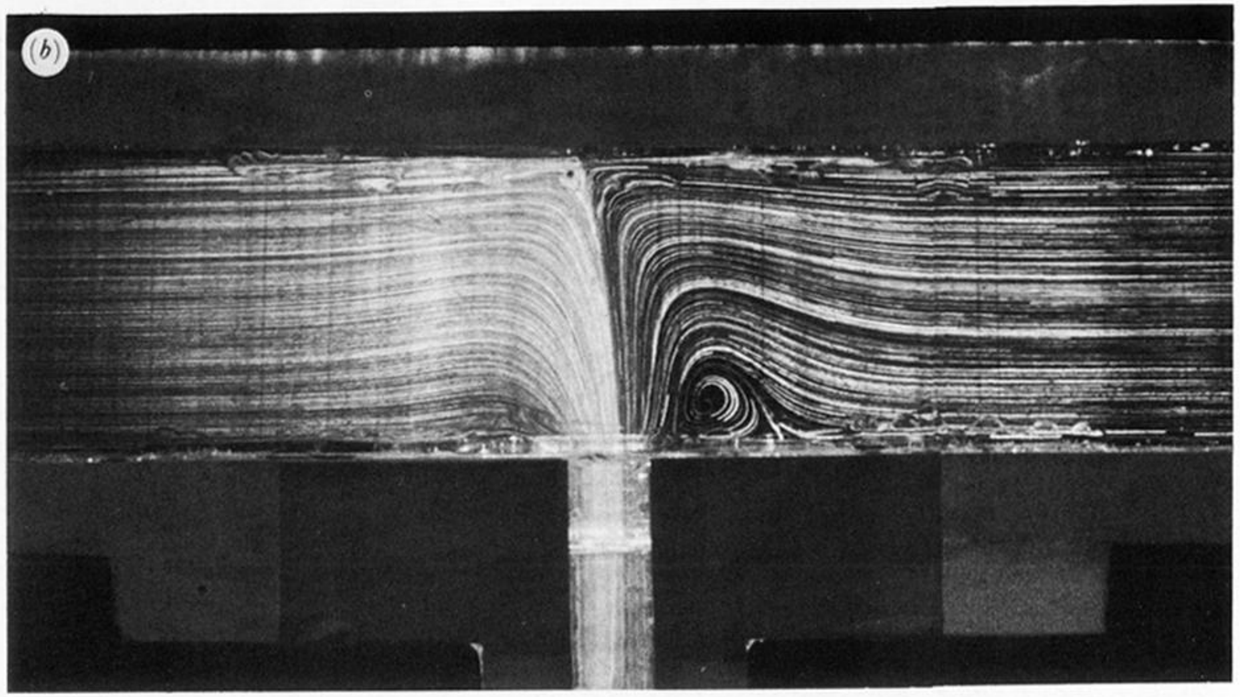

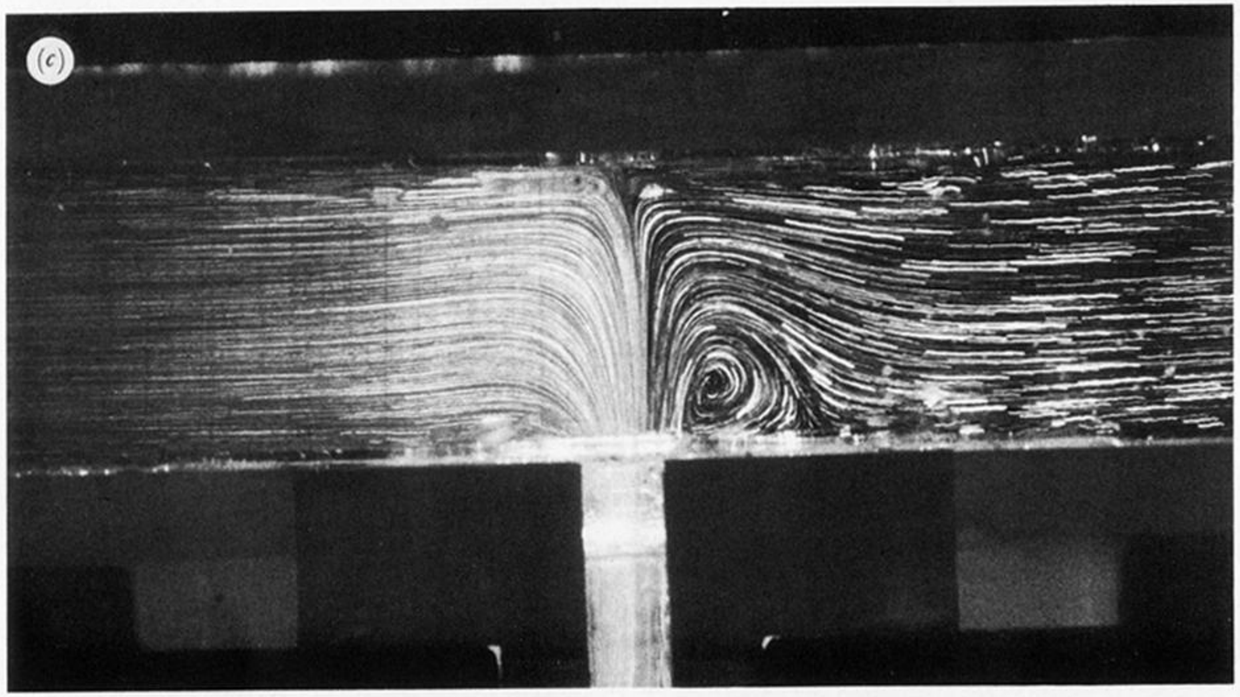

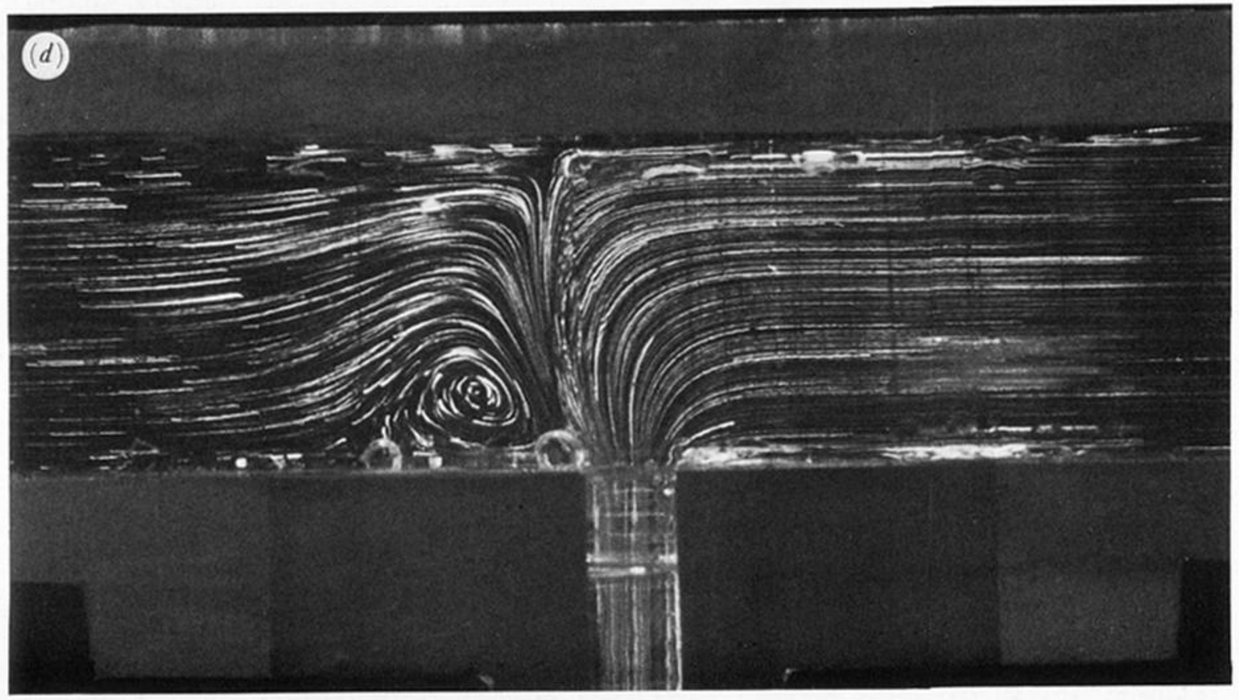

FIGURE 11. T geometry (3*a*) with Boger fluid and newtonian fluid entering through arms A and B respectively. (*a*) Fluid B44, $R_A = 0.018$, $W_A = 0.06$, and fluid N4, $R_B = 0.006$, $W_B \equiv 0$, total flow rate is 2.1 ml s^{-1}; (*b*) fluid B44, $R_A = 0.015$, $W_A = 0.052$, and fluid N4, $R_B = 0.024$, $W_B \equiv 0$, total flow rate is 2.8 ml s^{-1}; (*c*) fluid B44, $R_A = 0.015$, $W_A = 0.052$ and fluid N4, $R_B = 0.024$, $W_B \equiv 0$, total flow rate is 2.8 ml s^{-1}. Plane of laser near rear bounding wall. (*d*) Fluid B45, $R_A = 0.025$, $W_A = 0.002$ and fluid N5, $R_B = 0.037$, $W_B \equiv 0$, total flow rate is 1.0 ml s^{-1}.

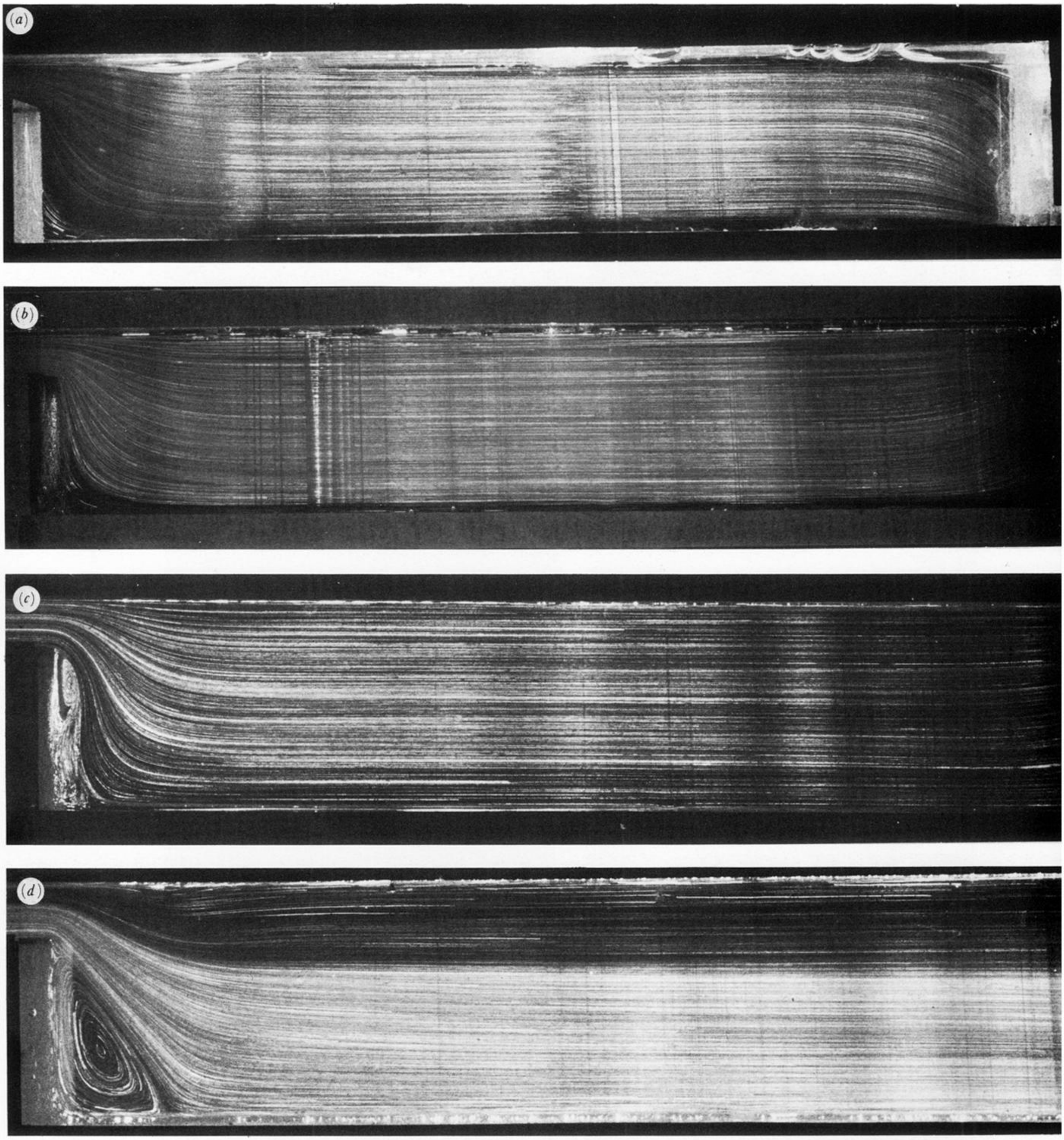

FIGURE 12. Flow patterns for one fluid flowing through the planar step geometry (3*c*). (*a*) newtonian fluid N8, $R = 0.058$, $W \equiv 0$, total flow rate is 13.2 ml s^{-1}; (*b*) Boger fluid B46, $R = 0.11$, $W = 0.027$, total flow rate is 5.5 ml s^{-1}; (*c*) Boger fluid B49, $R = 0.12$, $W = 0.048$, total flow rate is 6.6 ml s^{-1}; (*d*) Boger fluid B49, $R = 0.13$, $W = 0.052$, total flow rate is 7.1 ml s^{-1}.

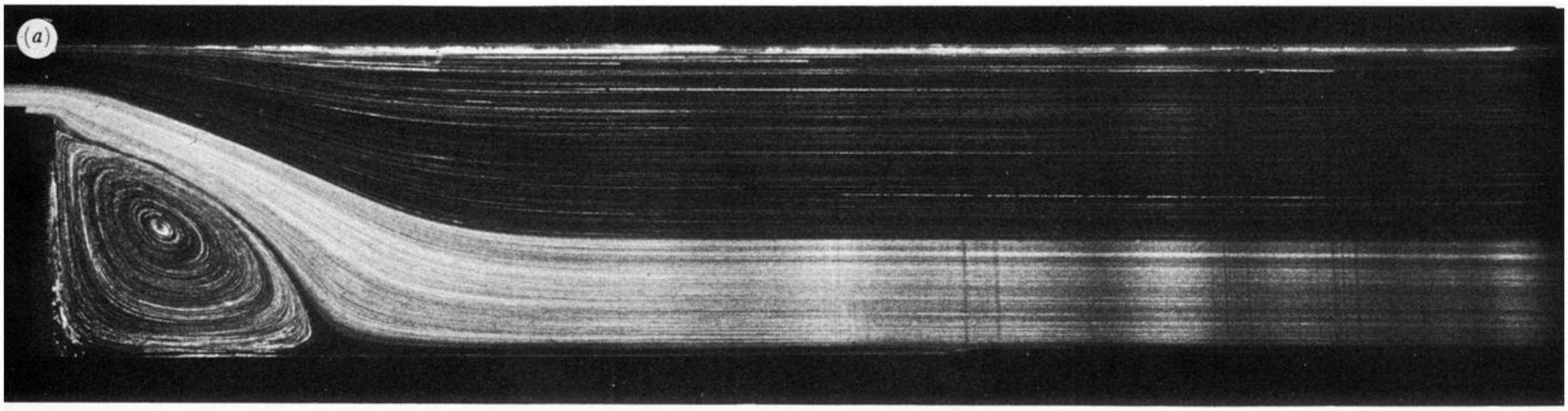

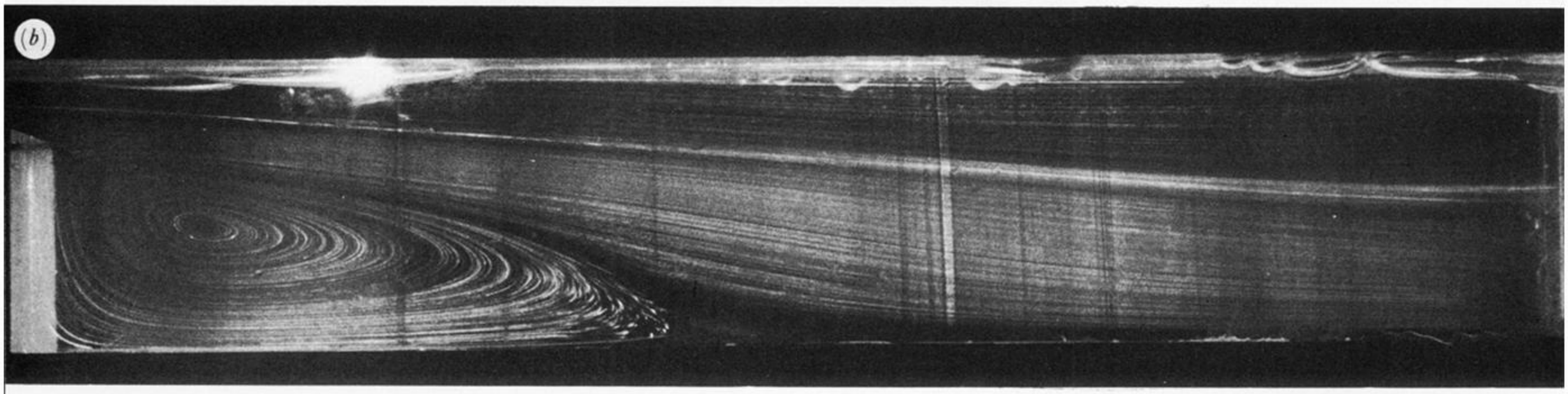

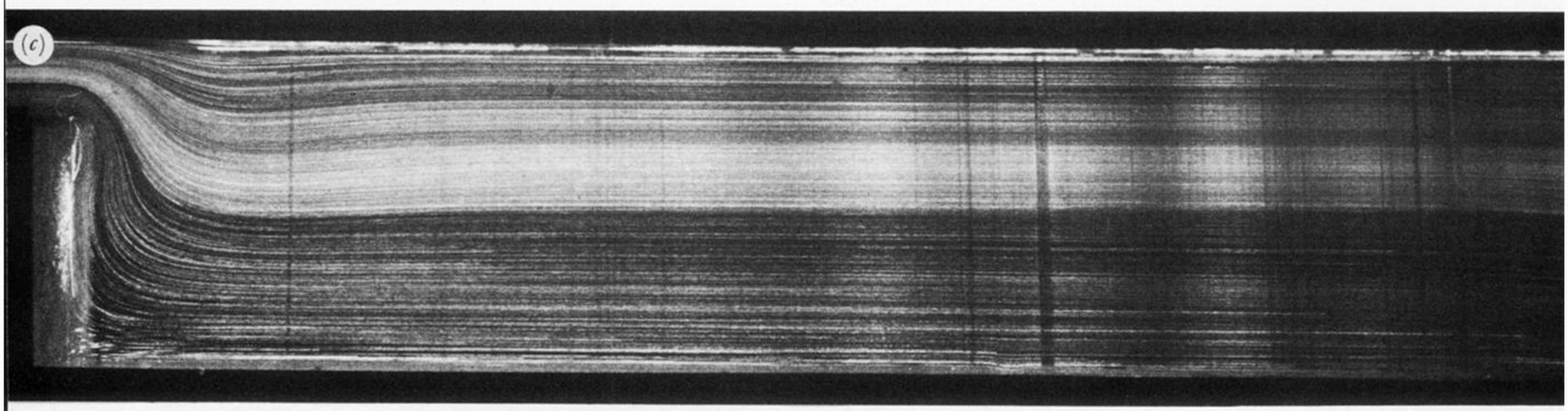

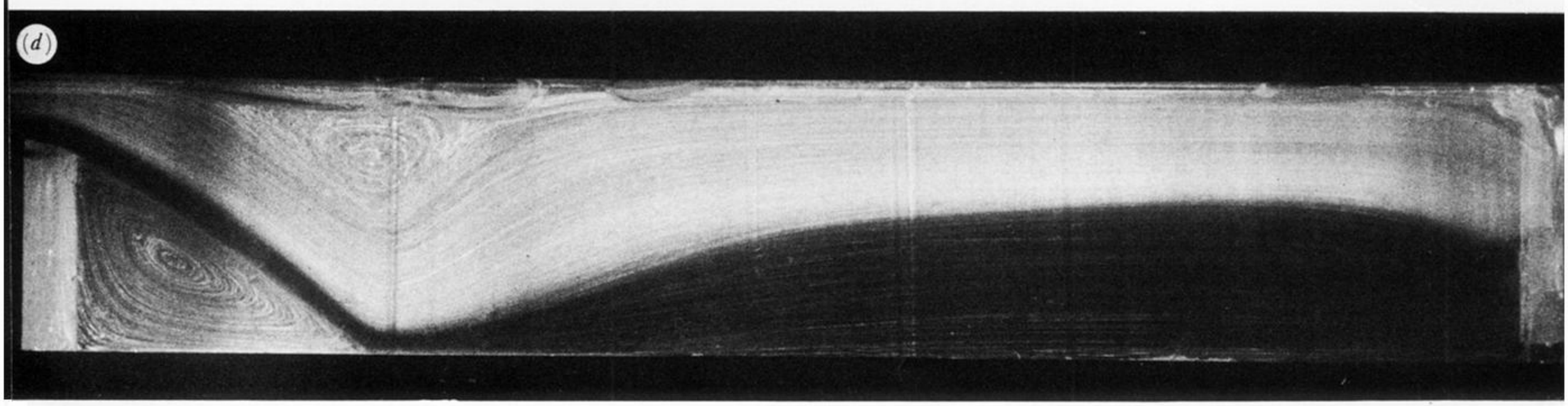

FIGURE 13. Flow patterns for two fluids flowing through the planar step geometry (3*c*). (*a*) Fluid 1 is B49, $Q_1 = 6.2$ ml s^{-1}, fluid 2 is N9, $Q_2 = 5.7$ ml s^{-1}; (*b*) fluid 1 is B47, $Q_1 = 11.8$ ml s^{-1}, fluid 2 is N8, $Q_2 = 13.2$ ml s^{-1}; (*c*) fluid 1 is N9, $Q_1 = 6.3$ ml s^{-1}, fluid 2 is B49, $Q_2 = 6.2$ ml s^{-1}; (*d*) fluid 1 is N8, $Q_1 = 19.7$ ml s^{-1}, fluid 2 is B47, $Q_2 = 11.8$ ml s^{-1}.

FIGURE 14. Flow patterns for two fluids flowing through the planar step geometry. (*a*) Fluid 1 is P, $Q_1 = 0.3$ ml s^{-1}, fluid 2 is B49, $Q_2 = 6.2$ ml s^{-1}; (*b*) fluid 1 is P, $Q_1 = 5.9$ ml s^{-1}, fluid 2 is B49, $Q_2 = 6.2$ ml s^{-1}; (*c*) fluid 1 is P, $Q_1 = 35.2$ ml s^{-1}, fluid 2 is B49, $Q_2 = 6.2$ ml s^{-1}.

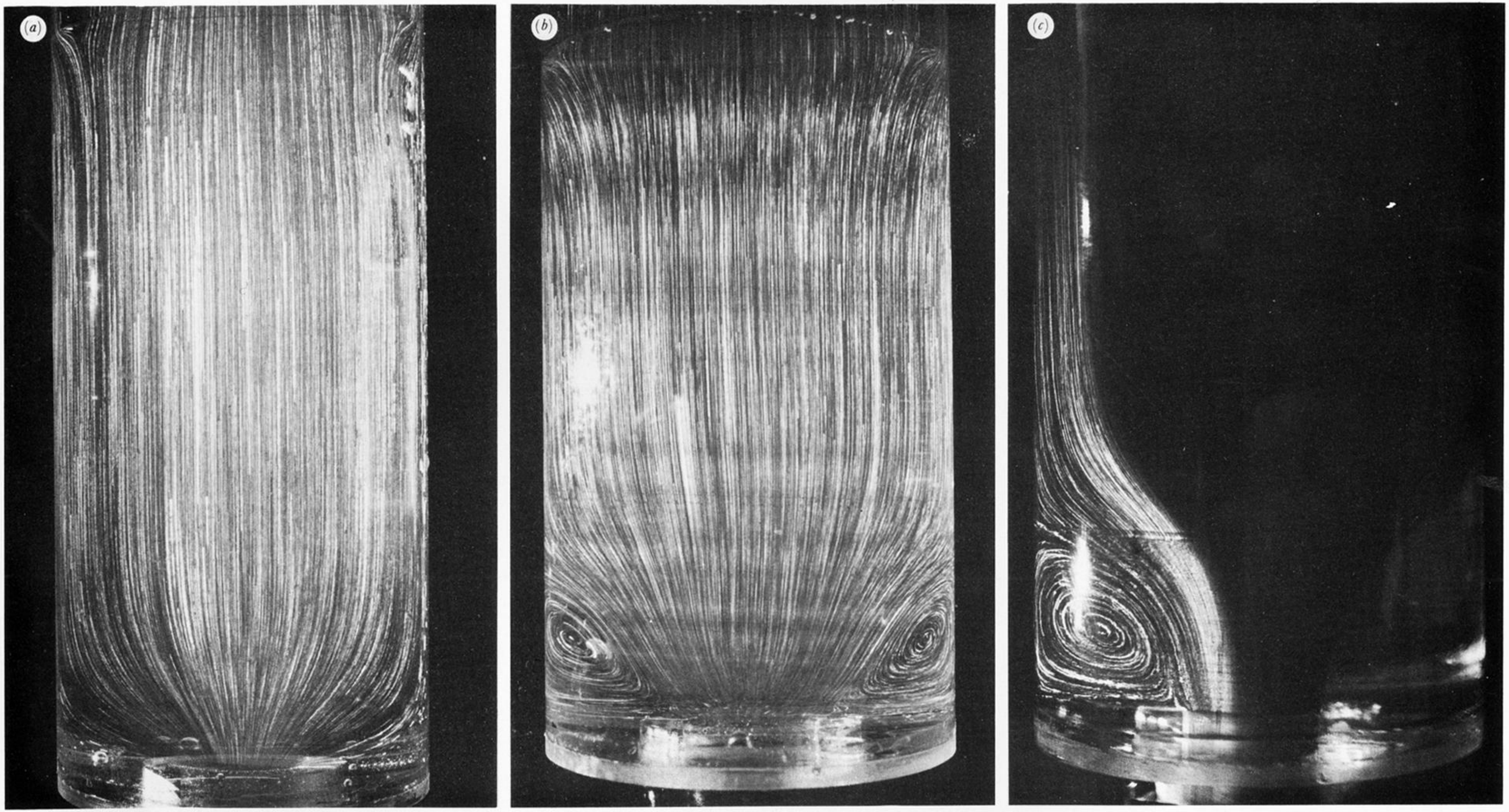

FIGURE 15. Flow patterns for fluids flowing in the axisymmetric geometry (3*d*). (*a*) One fluid, N6, flow rate is 8.1 ml s^{-1}; (*b*) one fluid, B46, flow rate is 18.5 ml s^{-1}; (*c*) fluid 1 is N6, flow rate is 8.0 ml s^{-1}, fluid 2 is B46, flow rate is 8.3 ml s^{-1}.